Lawrence Berkeley National Laboratory

Title
CONSTRAINED-TRANSPORT MAGNETOHYDRODYNAMICS WITH ADAPTIVE MESH REFINEMENT IN CHARM

Authors
Miniati, Francesco
Martin, Daniel F

Constrained-Transport Magnetohydrodynamics with Adaptive-Mesh-Refinement in CHARM

Francesco Miniati

Physics Department, Wolfgang-Pauli-Strasse 27, ETH-Zürich, CH-8093, Zürich, Switzerland; fm@phys.ethz.ch

Daniel F. Martin

Lawrence Berkeley National Laboratory, 1 Cyclotron Rd, Berkeley, CA 94720, USA; DFMartin@lbl.gov

ABSTRACT

We present the implementation of a three-dimensional, second order accurate Godunov-type algorithm for magneto-hydrodynamic (MHD), in the adaptive-mesh-refinement (AMR) cosmological code CHARM. The algorithm is based on the full 12-solve spatially unsplit Corner-Transport-Upwind (CTU) scheme. The fluid quantities are cell-centered and are updated using the Piecewise-Parabolic-Method (PPM), while the magnetic field variables are face-centered and are evolved through application of the Stokes theorem on cell edges via a Constrained-Transport (CT) method. The multidimensional MHD source terms required in the predictor step for high-order accuracy are applied in a simplified form which reduces their complexity in three dimensions without loss of accuracy or robustness. The algorithm is implemented on an AMR framework which requires specific synchronization steps across refinement levels. These include face-centered restriction and prolongation operations and a *reflux-curl* operation, which maintains a solenoidal magnetic field across refinement boundaries. The code is tested against a large suite of test problems, including convergence tests in smooth flows, shock-tube tests, classical two- and three-dimensional MHD tests, a three-dimensional shock-cloud interaction problem and the formation of a cluster of galaxies in a fully cosmological context. The magnetic field divergence is shown to remain negligible throughout.

Subject headings: cosmology: theory — methods: numerical — magnetohydrodynamics: MHD

1.   Introduction

Magnetic fields are a common feature of cosmic plasmas, from the interplanetary medium and the atmospheres of stars, to the interstellar medium of galaxies and the baryonic gas in the largest structures of the universe such as clusters and voids of galaxies (e.g., Zel'dovich et al. 1983; Bernet et al. 2008; Clarke et al. 2001; Neronov & Vovk 2010).

Their origin is discussed in several papers and different processes are likely responsible for the magnetization of different environments (see, e.g. Miniati & Bell 2011, and references therein). In general weak rotational electrostatic fields are required, which are normally suppressed by the high conductivity of astrophysical plasmas, but which can nevertheless arise under special conditions. The magnetic field can then evolve considerably and amplification of an initially weak seed by many orders of magnitude is plausible, particularly when the flow is highly turbulent (Zel'dovich et al. 1983). Magnetic fields affect the dynamics of a system directly through the Lorentz force and indirectly through their impact on the plasma microscopic properties, e.g. the thermal conductivity or electric resistivity (Spitzer 1965), or the transport of high energy particles (Schlickeiser 2002), both with conspicuous macroscopic effects. Thus magnetic fields are a crucial component of astrophysical plasmas although perhaps due to the complexity they introduce, progress in characterizing their role has been relatively slow, particularly in certain areas of astrophysics. Due to such complexities, particularly during highly nonlinear regimes, accurate and efficient numerical methods are valuable for studying the evolution of magnetized systems.

A simplified description of a magnetized fluid is provided by the equations of ideal magneto-hydrodynamics (MHD). This approximation is valid when the following hierarchy of scales is satisfied: $\ell_{mfp} \ll \lambda \ll L$, where ℓ_{mfp} is the mean-free-path of the fluid particles, λ is the characteristic scale of the problem of interest and L is the size of the system (Ginzburg 1979). The mfp can be suppressed considerably in the direction perpendicular to the magnetic field lines, but in parallel directions one relies typically on collisions to guarantee the fluid approximation. In reality microscopic plasma processes or a tangled component of the magnetic field can also provide the required viscosity. Notably the MHD approximation prevents the occurrence of kinetic processes which, however, can sometimes by represented by source terms on the RHS of the MHD equations.

When dissipative terms can be neglected, the MHD equations are in ideal form and

read (Landau & Lifshitz 1984)

$$\frac{\partial \rho}{\partial t} + \frac{\partial \rho u_j}{\partial x_j} = 0, \tag{1}$$

$$\frac{\partial \rho u_i}{\partial t} + \frac{\partial}{\partial x_j} \left(\rho u_i u_j + p \delta_{ij} - B_j B_i \right) = 0, \tag{2}$$

$$\frac{\partial \rho e}{\partial t} + \frac{\partial}{\partial x_j} \left[u_j \left(\rho e + p \right) - B_j B_i u_i \right] = 0. \tag{3}$$

Here ρ is the gas density, u_i and B_i the components of the velocity and magnetic field vectors, respectively, $p = p_g + \frac{1}{2} B^2$ is the total sum of the gas and magnetic pressures, $e = \frac{1}{2} u^2 + e_{th} + \frac{1}{2} \frac{B^2}{\rho}$ is the total specific energy density, δ_{ij} Kronecker's delta and summation over repeated indices is assumed. The thermal energy is related to the pressure through a γ-law equation of state, $e_{th} = p_g / \rho(\gamma - 1)$. The magnetic field evolution is described by Faraday's equation, with the electric field given by Ohm's law. In the limit of negligible resistivity the only electric fields are those induced by motions of the magnetized fluid and the induction equation reads (Landau & Lifshitz 1984)

$$\frac{\partial B_i}{\partial t} = -\varepsilon_{ijk} \frac{\partial E_k}{\partial x_j} = -\frac{\partial}{\partial x_j} \left(u_j B_i - B_j u_i \right), \tag{4}$$

where ε_{ijk} is the fully antisymmetric tensor of rank 3 and $\varepsilon_{012} = 1$.

The resistive terms neglected in Eq. (1)–(4), which are responsible for the diffusion of the magnetic field, can be readily recovered (Samtaney et al. 2005), although for most purposes their neglect is safe in astrophysical plasmas.

There are various approaches to solve numerically the equations of MHD. The one we follow in this paper is based on the extension to MHD of conservative methods for hyperbolic systems of equations, particularly Godunov's methods for hydrodynamics. This approach is met with two difficulties, however. First, care much be taken because the system of MHD equations is not strictly hyperbolic. This can be dealt with by "renormalizing" the eigenvalues and eigenvectors of the system (Brio & Wu 1988). Second, and most importantly the solenoidal constraint, $\nabla \cdot \mathbf{B} = 0$, must be enforced or else the solution will contain artifacts (Brackbill & Barnes 1980). Unfortunately numerical schemes designed for pure hydrodynamics do not fulfill such requirement and the above constraint must be enforced separately. Different ways to do so have been proposed. In one approach the magnetic field is defined together with all other fluid variables at cell centers and the non-solenoidal component is removed through a Hodge-Helmholtz projection method, typically once per time-step (Brackbill & Barnes 1980; Zachary et al. 1994; Ryu et al. 1995). In a variation of this approach the projection operation is performed on the magnetic field variables extrapolated to the cell faces which are used to define the MHD fluxes (Crockett et al. 2005). It

is argued in Crockett et al. (2005) that this type of projection is mathematically more consistent with the solenoidal requirement because it is the fluxes defined on the cell faces that get differentiated to compute the flux updates. In a second approach, the MHD equations are cast in a special 8-wave non-conservative formulation. This allows for the non-solenoidal component of the magnetic field to be explicitly tracked and suitably damped as it is advected by the flow (Powell et al. 1999; Dedner et al. 2002).

Finally in the Constrained Transport (CT) approach, the discretization strategy originally proposed by Yee (1966) in the context of Maxwell equations is used, in which the magnetic field is defined at face centers, the electric field used to update the latter is defined at cell edges, and the other fluid variables are defined at cell centers as in ordinary hydrodynamics (Evans & Hawley 1988; Dai & Woodward 1998; Ryu et al. 1998; Balsara & Spicer 1999; Tóth 2000; Londrillo & del Zanna 2004; Fromang et al. 2006; Cunningham et al. 2009). In this approach the rate of change of the magnetic flux at cell faces is given by the circulation of the electric field along the cell edges which define the boundary of the corresponding face. Thus the solenoidal character of the magnetic field is ensured by Stokes' theorem down to machine precision. Recently Gardiner & Stone (2005, 2008) have developed an unsplit version of the CT algorithm, extending to the case of MHD the Corner Transport Upwind (CTU) method for directionally unsplit hydrodynamics proposed in Colella (1990) and Saltzman (1994). The use of a directionally unsplit algorithm has proven quite attractive, particularly because it appears to be better suited for modeling turbulent flows (Bell et al) and in the presence of source terms (Leveque 1998). Most importantly, due to the solenoidal constraint, the MHD equations contain intrinsically multidimensional terms which require a directionally unsplit formulation if one is to achieve high order accuracy in multidimensional problems (Gardiner & Stone 2005). Thus the extension of CTU to MHD has also attracted considerable interest in the astrophysical community (e.g. Teyssier et al. 2006; Fromang et al. 2006; Lee & Deane 2009; Mignone & Tzeferacos 2010).

In this paper we describe the implementation of a version of the CTU + CT scheme that closely resembles the one of Gardiner & Stone (2008) and Stone et al. (2008). Our scheme differs from theirs, however, in two respects. First we have chosen to use the full 12-solve CTU scheme instead of the simpler 6-solve scheme. The reason for this choice is due to the larger CFL number that the full CTU scheme can afford (CFL=1), as compared to the simplified version (CFL=0.5). As indicated by Gardiner & Stone (2008) the computational cost of the two versions of the CTU scheme is roughly the same for pure MHD calculations, because the factor of two fewer Riemann solvers comes with twice as many steps to achieve the same solution time. However, for multi-physics applications that we have in mind other expensive solvers are executed each time step, whose cost grows with the number of time-steps. Note that Teyssier et al. (2006) use also a simpler version of the CTU scheme, although in their

case a slightly less restrictive condition on the time-step is nominally allowed, i.e. CFL≤ 0.7. On the other hand, Lee & Deane (2009) have introduced a different approach for computing the transverse flux updates of the fluid variables in their directionally unsplit method, which relies on characteristic tracing alone and does not require intermediate Riemann solvers (except for the magnetic field intermediate updates). For this reason and since the stability constraint only requires CFL≤ 1 this approach can potentially be quite efficient.

Secondly, we take into account the multidimensional corrections required to balance the $\nabla \cdot \mathbf{B}$ terms in a form that is simpler than originally proposed by Gardiner & Stone (2008), and analogous to Crockett et al. (2005). Our tests suggest that the accuracy and robustness of the algorithm are not affected by this simplification.

Finally, using in particular the ideas in Berger & Colella (1989) for adaptive-mesh-refinement (AMR) and Balsara (2001) for the divergence-free coarse-fine interpolation of the magnetic field in newly refined grid patches, we have implemented an AMR version of our CTU + CT MHD scheme. The code in which the implementation is carried out is CHARM (Miniati & Colella 2007a). It includes various other physical modules, namely self-gravity, collision-less dark matter particles and cosmic expansion for cosmological applications, radiative cooling (Miniati & Colella 2007b), cosmic-rays (Miniati 2001, 2007) and dust particles (Miniati 2010).

The remainder of this paper is organized as follows. The algorithm is discussed in detail in Sec. 2. In Sec 3 we present results for an extensive set of problems that test the accuracy and robustness of the code. These tests include a convergence study in smooth flows, a suite of Riemann problems in one and two dimensions, the Orszag-Tang Vortex as well as the rotor problem, carried out on a uniform grid. Finally, extension to AMR and to the case of cosmological applications are described in Sec. 4 and 5, respectively. We have tested these extensions with a problem involving the interaction of a magnetized interstellar cloud with a strong shock, and the formation of a galaxy cluster in a fully cosmological simulation. The paper closes with a brief summary in Sec. 6.

2. Numerical Scheme

In this section we first provide an overall description of the full CTU + CT algorithm and, following that, we discuss the implementation details. We begin by a description of the space discretization, data structure and notation.
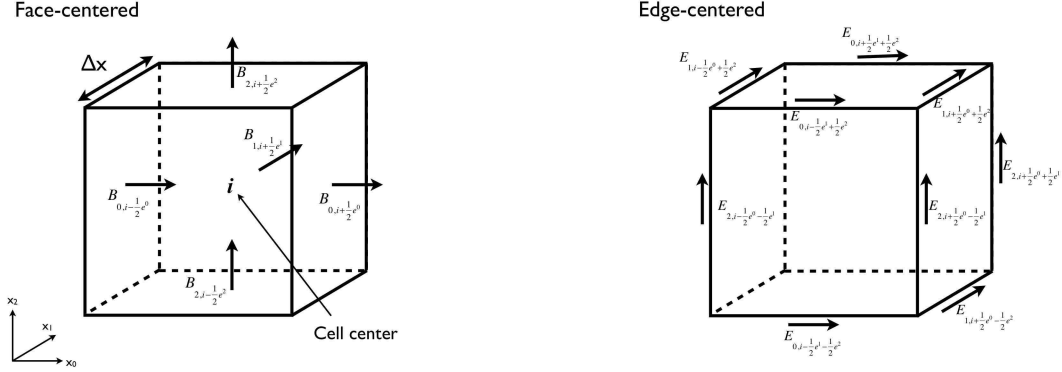
Fig. 1.— Control volume and discrete representation of physical quantities.

2.1. Preliminaries

2.1.1. Discretization, Variables and Operators

The algorithmic operations are carried out on a discrete representation of the continuous **D**-dimensional space given by the cubic lattice, $\boldsymbol{i} \equiv (i_0, ..., i_{\mathbf{D}-1}) \in \mathbb{Z}^{\mathbf{D}}$. The computational domain, referred to as a grid Γ, is a bound subset of $\mathbb{Z}^{\mathbf{D}}$ and provides a finite-volume discretization of the continuous space into a collection of control volumes, faces and edges. Each control volume is identified by an index $\boldsymbol{i} \equiv (i_0, ..., i_{\mathbf{D}-1}) \in \Gamma$ and corresponds to a region of space,

$$V_{\boldsymbol{i}} = [\boldsymbol{i}h, (\boldsymbol{i} + \boldsymbol{v})h], \tag{5}$$

where h is the mesh spacing, and $\boldsymbol{v} \equiv (1, ..., 1)$ is the vector whose components are all equal to one. The face-centered discretization of space based on the same control volumes is: $\Gamma_{\mathrm{f}}^{\boldsymbol{e}^d} = \{\boldsymbol{i} \pm \frac{1}{2}\boldsymbol{e}^d : \boldsymbol{i} \in \Gamma\}$, where $\boldsymbol{e}^d$ is the unit vector in the d direction. $\Gamma_{\mathrm{f}}^{\boldsymbol{e}^d}$ indexes the cell faces of Γ normal to $\boldsymbol{e}^d$ representing the areas

$$A_{\boldsymbol{i}+\frac{1}{2}\boldsymbol{e}^d} = [(\boldsymbol{i} + \boldsymbol{e}^d)h, (\boldsymbol{i} + \boldsymbol{v})h], \quad \boldsymbol{i} + \frac{1}{2}\boldsymbol{e}^d \in \Gamma_{\mathrm{f}}^{\boldsymbol{e}^d}. \tag{6}$$

Finally, the edge-centered discretization of space is: $\Gamma_{\mathrm{e}}^{\boldsymbol{e}^d} = \{\boldsymbol{i} \pm \frac{1}{2}\boldsymbol{e}^{d_1} \pm \frac{1}{2}\boldsymbol{e}^{d_2} : \boldsymbol{i} \in \Gamma,\, d \neq d_1 \neq d_2\}$. $\Gamma_{\mathrm{e}}^{\boldsymbol{e}^d}$ indexes the edges of the cells in Γ aligned with $\boldsymbol{e}^d$ representing the lengths

$$L_{\boldsymbol{i}+\frac{1}{2}(\boldsymbol{e}^{d_1}+\boldsymbol{e}^{d_2})} = [\boldsymbol{i}h + \frac{1}{2}(\boldsymbol{e}^{d_1} + \boldsymbol{e}^{d_2}), (\boldsymbol{i} + \boldsymbol{v})h], \quad \boldsymbol{i} + \frac{1}{2}(\boldsymbol{e}^{d_1} + \boldsymbol{e}^{d_2}) \in \Gamma_{\mathrm{e}}^{\boldsymbol{e}^d}. \tag{7}$$

Fig. 1 illustrates a control volume with the various types of discretization.

Given the above discretization, we define cell-centered discrete variables on Γ as

$$\phi : \Gamma \to \mathbb{R}^m,$$

and denote by $\phi_{\boldsymbol{i}} \in \mathbb{R}^m$ the value of ϕ at cell $\boldsymbol{i} \in \Gamma$. Similarly we define face-centered vector fields on $\Gamma_{\mathrm{f}}^{\boldsymbol{e}^d}$ as

$$\vec{F} = (F_0, \ldots, F_{\mathbf{D}-1}) \ , \ F_d : \Gamma_{\mathrm{f}}^{\boldsymbol{e}^d} \to \mathbb{R}^m,$$

and denote by $F_{d,\boldsymbol{i}+\frac{1}{2}\boldsymbol{e}^d} \in \mathbb{R}^m$ the value of F_d at $\boldsymbol{i} + \frac{1}{2}\boldsymbol{e}^d \in \Gamma_{\mathrm{f}}^{\boldsymbol{e}^d}$, and also define edge-centered vector fields on $\Gamma_{\mathrm{e}}^{\boldsymbol{e}^d}$ as

$$\vec{E} = (E_0, \ldots, E_{\mathbf{D}-1}) \ , \ E_d : \Gamma_{\mathrm{e}}^{\boldsymbol{e}^d} \to \mathbb{R}^m$$

and denote by $E_{d,\boldsymbol{i}+\frac{1}{2}(\boldsymbol{e}^{d_1}+\boldsymbol{e}^{d_2})} \in \mathbb{R}^m$ the value of E_d at $\boldsymbol{i} + \frac{1}{2}(\boldsymbol{e}^{d_1} + \boldsymbol{e}^{d_2}) \in \Gamma_{\mathrm{e}}^{\boldsymbol{e}^d}$. Finally, for face-centered fields we introduce the discretized divergence operator

$$\left(\vec{D} \cdot \vec{F} \right)_{\boldsymbol{i}} = \frac{1}{h} \sum_{d=0}^{\mathbf{D}-1} \left(F_{d,\boldsymbol{i}+\frac{1}{2}\boldsymbol{e}^d} - F_{d,\boldsymbol{i}-\frac{1}{2}\boldsymbol{e}^d} \right), \boldsymbol{i} \in \Gamma, \tag{8}$$

and for edge-centered fields the discretized curl operator

$$\left(\vec{D} \times \vec{E} \right)_{d,\boldsymbol{i}+\frac{1}{2}\boldsymbol{e}^d} = \frac{1}{h} \sum_{d_1,d_2} \varepsilon_{dd_1d_2} \left(E_{d_1,\boldsymbol{i}+\frac{1}{2}\boldsymbol{e}^d+\frac{1}{2}\boldsymbol{e}^{d_2}} - E_{d_1,\boldsymbol{i}+\frac{1}{2}\boldsymbol{e}^d-\frac{1}{2}\boldsymbol{e}^{d_2}} \right), \quad \boldsymbol{i} + \frac{1}{2}\boldsymbol{e}^d \in \Gamma_{\mathrm{f}}^{\boldsymbol{e}^d}. \tag{9}$$

Time is also discretized into a number of finite intervals of variable size. In particular, we write $t^{n+1} = t^n + \Delta t^n$, where t indicates the solution time, n indicates the integration step, and Δt^n the time-step interval.

2.1.2. Time Integration

The coupled system of equations (1)-(4), with the allowance for a non-zero source term $S(U)$, can be cast in the following compact form

$$\frac{\partial U}{\partial t} + \nabla \cdot \mathbf{F} = S, \tag{10}$$

where the conservative variables, U, and the associated fluxes along the direction d, F_d, are defined as

$$
U = \begin{pmatrix} \rho \\ \rho u_0 \\ \vdots \\ \rho u_{\mathbf{D}-1} \\ \rho e \\ B_0 \\ \vdots \\ B_{\mathbf{D}-1} \end{pmatrix}, \quad F_d(U) = \begin{pmatrix} \rho u_d \\ \rho u_0 u_d + p\,\delta_{d0} - B_0 B_d \\ \vdots \\ \rho u_{\mathbf{D}-1} u_d + p\,\delta_{d\mathbf{D}-1} - B_{\mathbf{D}-1} B_d \\ u_d\,(\rho e + p) - B_d \mathbf{B} \cdot \mathbf{u} \\ u_0 B_d - B_0 u_d \\ \vdots \\ u_{\mathbf{D}-1} B_d - B_{\mathbf{D}-1} u_d \end{pmatrix}. \tag{11}
$$

Following Godunov's approach and its higher order extensions, we can conveniently formulate a numerical integration scheme based on the conservative properties of the system (10). In this approach one follows the evolution of cell-centered volume-averaged conservative variables, defined as

$$
U_{\boldsymbol{i}}^n = \frac{1}{V_{\boldsymbol{i}}} \int_{V_{\boldsymbol{i}}} U(t^n, \boldsymbol{x})\,dV. \tag{12}
$$

The evolution equation is obtained upon suitable manipulation of the original continuous Eq. (10), and reads (Leveque 1998)

$$
U_{\boldsymbol{i}}^{n+1} = U_{\boldsymbol{i}}^n - \frac{\Delta t}{\Delta x} \sum_{d=0}^{\mathbf{D}-1} \left(F_{d,\boldsymbol{i}+\frac{1}{2}\boldsymbol{e}^d}^{n+\frac{1}{2}} - F_{d,\boldsymbol{i}-\frac{1}{2}\boldsymbol{e}^d}^{n+\frac{1}{2}} \right) + S^{n+\frac{1}{2}}, \tag{13}
$$

where the face-centered time-averaged fluxes along the direction d are defined as

$$
F_{d,\boldsymbol{i}+\frac{1}{2}\boldsymbol{e}^d}^{n+\frac{1}{2}} = \frac{1}{\Delta t A_{\boldsymbol{i}+\frac{1}{2}\boldsymbol{e}^d}} \int_{t^n}^{t^{n+1}} dt \int_{A_{\boldsymbol{i}+\frac{1}{2}\boldsymbol{e}^d}} F_d(t, \boldsymbol{x})\,dA. \tag{14}
$$

If the source term is non-stiff, we can obtain a second order estimate for it by the simple time-average, $S^{n+\frac{1}{2}} \simeq \frac{1}{2}(S^n + S^{n+1})$.

Note that given the flux along a direction d_1, $F_{d_1,\boldsymbol{i}+\frac{1}{2}\boldsymbol{e}^{d_1}}$, the component corresponding to the magnetic field along the direction $d_2 \neq d_1$, defines a face centered electric field along d according to

$$
E_{d,\boldsymbol{i}+\frac{1}{2}\boldsymbol{e}^{d_1}} = -\varepsilon_{dd_1d_2}\, F_{d_1,\boldsymbol{i}+\frac{1}{2}\boldsymbol{e}^{d_1}}^{B_{d_2}}(U), \tag{15}
$$

where we use subscripts to indicate directions and centering, and superscripts for components. Indeed, Godunov's scheme also updates in time the cell-centered magnetic fields variables. As already pointed out, however, the updated magnetic field in general does not

remain solenoidal. Therefore, we adopt instead a CT discretization strategy in which the primary description of the magnetic field we will be using face-centered area-averaged variables defined as

$$B^n_{d,\boldsymbol{i}+\frac{1}{2}\boldsymbol{e}^d} = \frac{1}{A_{\boldsymbol{i}+\frac{1}{2}\boldsymbol{e}^d}} \int_{A_{\boldsymbol{i}+\frac{1}{2}\boldsymbol{e}^d}} B_d(t^n, \boldsymbol{x})\, dA. \tag{16}$$

Note that an estimate of the cell-centered magnetic field variables is still needed in order to construct the fluxes in (14). We will return to this point shortly. The evolution equation for the face-centered magnetic field variables is obtained again from a manipulation of Faraday's law and reads

$$
\begin{aligned}
B^{n+1}_{d,\boldsymbol{i}+\frac{1}{2}\boldsymbol{e}^d} = B^n_{d,\boldsymbol{i}+\frac{1}{2}\boldsymbol{e}^d} &- \varepsilon_{dd_1d_2} \frac{\Delta t}{\Delta x} \left[\left(E^{n+\frac{1}{2}}_{d_1,\boldsymbol{i}+\frac{1}{2}\boldsymbol{e}^d+\frac{1}{2}\boldsymbol{e}^{d_2}} - E^{n+\frac{1}{2}}_{d_1,\boldsymbol{i}+\frac{1}{2}\boldsymbol{e}^d-\frac{1}{2}\boldsymbol{e}^{d_2}} \right) \right. \\
&\left. - \left(E^{n+\frac{1}{2}}_{d_2,\boldsymbol{i}+\frac{1}{2}\boldsymbol{e}^d+\frac{1}{2}\boldsymbol{e}^{d_1}} - E^{n+\frac{1}{2}}_{d_2,\boldsymbol{i}+\frac{1}{2}\boldsymbol{e}^d-\frac{1}{2}\boldsymbol{e}^{d_1}} \right) \right] \\
&+ S^{n+\frac{1}{2}}_{B_d,\boldsymbol{i}+\frac{1}{2}\boldsymbol{e}^d}
\end{aligned}
\tag{17}
$$

with $d \neq d_1 \neq d_2, 0 \leq d, d_1, d_2 < \mathbf{D}$. The edge-centered time-averaged electric field is formally defined as

$$E^{n+\frac{1}{2}}_{d,\boldsymbol{i}+\frac{1}{2}\boldsymbol{e}^{d_1}+\frac{1}{2}\boldsymbol{e}^{d_2}} = \frac{1}{\Delta t\, L_{\boldsymbol{i}+\frac{1}{2}(\boldsymbol{e}^{d_1}+\boldsymbol{e}^{d_2})}} \int_{t^n}^{t^{n+1}} dt \int_{L_{\boldsymbol{i}+\frac{1}{2}(\boldsymbol{e}^{d_1}+\boldsymbol{e}^{d_2})}} E_d(t, \boldsymbol{x})\, dL. \tag{18}$$

and, as above, the time-centered estimate of the non-stiff source term for the face-centered magnetic field components is obtained by simple arithmetic averaging. The cell-centered magnetic field variables are then defined in terms of the primary face-centered values using the following second-order accurate reconstruction scheme (Ryu et al. 1998; Balsara 2001; Gardiner & Stone 2005)

$$B_{d,\boldsymbol{i}} = \frac{1}{2} \left(B_{d,\boldsymbol{i}-\frac{1}{2}\boldsymbol{e}^d} + B_{d,\boldsymbol{i}+\frac{1}{2}\boldsymbol{e}^d} \right). \tag{19}$$

An important part of CT schemes concerns the calculation of the time-averaged, edge-centered electric fields entering the time update (17). In general one employs some type of bilinear interpolation. Dai & Woodward (1998) interpolate in space and time the cell-centered velocity and magnetic field at time t^n with the solution from the Godunov scheme at time t^{n+1} to obtain time- and corner-centered electric fields. On the other hand, Ryu et al. (1998) and Balsara (2001) take advantage of Eq. (15) and interpolate the face-centered variables that allow reconstruction of electric fields at cell edges. The interpolation scheme proposed in Ryu et al. (1998) has the property that for plane-parallel configurations their multidimensional scheme reduces to the one-dimensional scheme. This same property is shared by the upwind scheme proposed in Gardiner & Stone (2005) which is adopted here and

is described in more detail in Sec. 2.2.6. This property is important because it guarantees self-consistency between (a) the electric fields used for the time-update of face-centered magnetic variables, (b) the MHD fluxes used for the time-update of the cell-centered variables and (c) the synchronization step of the magnetic variables given in Eq. (19) (Gardiner & Stone 2005).

Note that by applying the divergence operator in Eq. (8) to the face-centered magnetic field evolved according to Eq. (17), one finds that the divergence of the field does not change in time. So the magnetic field remains solenoidal if initially so. This is the property of the CT scheme.

The accuracy and stability of the numerical solution depend principally on how the time-averaged fluxes and electric fields entering Eq. (13) and (17), respectively, are computed. In the following sections we shall describe the algorithmic details characterizing such calculation.

2.2. Algorithm

The algorithm described in this section computes second-order accurate face centered fluxes and edge-centered electric fields required for the update of the cell-centered fluid variables and face-centered magnetic field variables in Eq.(13) and (17), respectively. It uses a combination of the CTU algorithm (Colella 1990; Saltzman 1994), and the CT scheme, as in Gardiner & Stone (2008). Unlike these authors, though, for the reasons indicated in the Introduction we will employ the full CTU scheme with 12-solve per cells (in 3-dimensions).

Assuming the solution at time t^n, $U_{\boldsymbol{i}}^n$ to be known, the outline of the algorithm is as follows:

1. transform from conservative to primitive variables, $U_{\boldsymbol{i}}^n \leftarrow W_{\boldsymbol{i}}^n$, and synchronize cell-centered and face-centered magnetic field values

2. compute limited slopes along the coordinate directions, $\delta W_{\boldsymbol{i},d}^n$.

3. do characteristic tracing to extrapolate in space and time primitive variables from cell centers to cell faces, $W_{\boldsymbol{i},\pm,d}$. Also include effects of source term here.

4. convert back to conservative variables, $W_{\boldsymbol{i},\pm,d} \leftarrow U_{\boldsymbol{i},\pm,d}$.

5. apply corrections to $U_{\boldsymbol{i},\pm,d}$ due to transverse gradients and obtain multidimensionally correct time-averaged fluxes $F_{\boldsymbol{i}+\frac{1}{2}\boldsymbol{e}^d}^{n+\frac{1}{2}}$ and electric fields $E_{\boldsymbol{i}+\frac{1}{2}\boldsymbol{e}^{d_1}+\frac{1}{2}\boldsymbol{e}^{d_2}}^{n+\frac{1}{2}}$.

6. update primary variables, $U_{\boldsymbol{i}}^n \leftarrow U_{\boldsymbol{i}}^{n+1}$ and $B_{\boldsymbol{i}+\frac{1}{2}\boldsymbol{e}^d}^n \leftarrow B_{\boldsymbol{i}+\frac{1}{2}\boldsymbol{e}^d}^{n+1}$ and synchronize cell-centered and face-centered magnetic field values.

7. update solution time $t \leftarrow t + \Delta t$ and compute new timestep according to the Courant-Friedrichs-Lewy (CFL) condition for stability,

$$\Delta t \leftarrow C_{\mathrm{CFL}} \frac{\Delta x}{\mathrm{Max}(u_{\boldsymbol{i},d}^{n+1} + c_{f,\boldsymbol{i}}^{n+1})}, \tag{20}$$

where the CFL number is, $C_{\mathrm{CFL}} < 1$, u_d is the $d-$component of the velocity field, c_f is the fast magnetosonic wave speed and the max value is computed over all directions d and over all cells in the computational domain.

In the following subsections we provide additional details about the algorithm.

2.2.1. Primitive Variables

The first part of the algorithm consists in reconstructing the numerical solution within the spatial domain of the mesh. This requires estimating gradients and eventually extrapolating state variables in time and space from cell centers to cell faces with the use of characteristic tracing. Such operations are usually done in *primitive* space, where the variables are defined as

$$W = (\rho, u_0, \ldots, u_{\mathbf{D}-1}, p_g, B_0, \ldots, B_{\mathbf{D}-1})^T, \tag{21}$$

as it simplifies the characteristic analysis of the system. The evolution of the system in terms of primitive variables is given by a system of equations in non-conservative form,

$$\frac{\partial W}{\partial t} + \sum_{d=0}^{\mathbf{D}-1} A_d(W) \frac{\partial W_d}{\partial x_d} = S^W, \tag{22}$$

where $S^W = \nabla_U W \cdot S$ and $A_d = \nabla_U W \cdot \nabla_U F_d \cdot \nabla_W U$, and $\nabla_U W$ and $\nabla_U W$ are the Jacobian of the transformation from primitive to conserved variables and vice-versa. Given their importance for the construction of a sound numerical scheme, the properties of the operators A_d have been studied in great details in the literature (e.g. Brio & Wu 1988; Roe & Balsara 1996). Here it suffices to make the following observations. In one dimension, $d = 0$, the parallel component of the magnetic field is constant, $B_0 = const.$, and A_0 effectively becomes a 7×7 matrix. In general the operator A_0 is characterized by 7 eigenvalues, and associated left and right eigenvectors, with values u, $u \pm c_s$, $u \pm c_A$ and $u \pm c_f$ obeying the hierarchy: $c_s \leq c_A \leq c_f$. The first eigenvalue listed above corresponds to the usual entropy wave, and the

other six to the three pairs of MHD waves (slow magnetosonic, Alfvén and fast magnetosonic) propagating downstream (+) or upstream (-) in the flow, respectively. Because up to 5 of the eigenvalues may actually coincide, the system is not strictly hyperbolic, so care must be taken to avoid singularities with expressions involving the eigenvectors (Brio & Wu 1988; Roe & Balsara 1996). Finally, in more then one dimensions, because B_d is not affected by gradients in the d direction, it has been customary to use the one-dimensional analysis when formulating the predictor step for higher-order Godunov-like MHD algorithms. However, that leads to neglect of terms $\propto \partial B_d/\partial x_d$, which are not necessarily null in multidimensions. In fact, it is important to include these terms to avoid degrading the solution accuracy, as recently pointed out by Gardiner & Stone (2005).

2.2.2. Slopes

After the conversion from conservative to primitive variables, $U_{\boldsymbol{i}}^n \leftarrow W_{\boldsymbol{i}}^n(U_{\boldsymbol{i}}^n)$ and the synchronization of cell-centered and face-centered magnetic fields according to Eq. (19), we proceed to the calculation of the slopes along each direction d as follows. First, central and side slopes are estimated, respectively, as

$$\delta_{d,0}W_{\boldsymbol{i}} = \frac{1}{2}\left(W_{\boldsymbol{i}+\boldsymbol{e}^d}^n - W_{\boldsymbol{i}-\boldsymbol{e}^d}^n\right), \tag{23}$$

$$\delta_{d,-}W_{\boldsymbol{i}} = W_{\boldsymbol{i}}^n - W_{\boldsymbol{i}-\boldsymbol{e}^d}^n, \tag{24}$$

$$\delta_{d,+}W_{\boldsymbol{i}} = W_{\boldsymbol{i}+\boldsymbol{e}^d}^n - W_{\boldsymbol{i}}^n, \tag{25}$$

and then *limiting* is applied component-wise either in primitive or in characteristic space. We use van Leer's limiter defined as

$$\delta^{vL}(\delta_0, \delta_-, \delta_+) = \begin{cases} \mathrm{sgn}(\delta_0) \ \min(|\delta_0|, 2|\delta_-|, 2|\delta_+|) & \text{if } \delta_-\delta_+ > 0 \\ 0 & \text{otherwise.} \end{cases}$$

In the case of primitive limiting the limiter is applied directly to each component k of the primitive slopes (23)-(25), i.e.

$$\delta_d W_{\boldsymbol{i}}^k = \delta^{vL}(\delta_{d,0}W_{\boldsymbol{i}}^k, \delta_{d,-}W_{\boldsymbol{i}}^k, \delta_{d,+}W_{\boldsymbol{i}}^k). \tag{26}$$

In the case of characteristic limiting the limiter is applied to the components of the primitive slopes in characteristic space, namely

$$\delta_d W_{\boldsymbol{i}} = \sum_k \alpha^k r^k, \tag{27}$$

$$\alpha^k = \delta^{vL}(\alpha_0^k, \alpha_-^k, \alpha_+^k), \tag{28}$$

$$\alpha_\#^k = l^k \cdot \delta_{d,\#}W_{\boldsymbol{i}}, \quad \# = 0, +, -, \tag{29}$$

where, $l^k = l^k(W_i^n)$ and $r^k = r^k(W_i^n)$ are the left and right eigenvectors of the operator $A_{i,d}$.

2.2.3. Normal Predictor

Next we extrapolate the primitive variables from cell centers to face centers along each coordinate direction, d, by taking into account the time-averaged effect due to the slopes just computed. This is done most conveniently by using the 1-D versions of the MHD equations in primitive form. There is no evolution in the $d-$component of the magnetic field due to derivatives along the $d-$direction, so the normal components of the magnetic field on cell faces are straightforwardly provided by the face-centered component of the magnetic field, without need for even geometrical extrapolation. On the other hand, as pointed out by Gardiner & Stone (2005) in multidimensional MHD the reconstruction step must include terms proportional to $\partial B_d/\partial x_d$ terms (no summation over repeated indices is implied here). These terms arise from the requirement to balance the divergence terms in more than one dimension and their neglect can cause serious degradation of the numerical solution. The reconstruction of the primitive variables onto cell faces can be done with various degrees of accuracy. Typically, one uses a piecewise-linear (PLM) or piecewise-parabolic (PPM) reconstruction scheme (Colella & Woodward 1984). Although we mostly use a PPM algorithm for the tests presented here, for simplicity we illustrate the case of PLM reconstruction. So in this case the extrapolation of the primitive variables in space and time from cell centers to faces along the direction d takes the form

$$\begin{pmatrix} \hat{W}_{i,\pm,d}^n \\ B_{d,i,\pm,d}^n \end{pmatrix} = \begin{pmatrix} \hat{W}_i^n \\ B_{d,i+e^d}^n \end{pmatrix} + \frac{1}{2}\left[\begin{pmatrix} \pm I & 0 \\ 0 & 0 \end{pmatrix} - \frac{\Delta t}{\Delta x}\begin{pmatrix} \hat{A}_{i,d} \\ 0 \end{pmatrix} P_\pm(\delta_d \hat{W}_i^n) \right] + \frac{\Delta t}{2}\begin{pmatrix} S_{d,i}^{n,\mathrm{MHD}} \\ 0 \end{pmatrix}.$$

(30)

where we have explicitly separated out the reconstruction of the normal component of the magnetic field (the *hat* symbol in the notation indicates that the components corresponding to the normal magnetic field are omitted). In addition, we have used the projector operator defined as

$$P_\pm(W) = \sum_{\pm\lambda_k>0} (l_k \cdot W)r_k$$

(31)

where λ_k are eigenvalues of $A_{i,d}$. This projector operator filters out the components of the gradients that propagate away from the cell interface. However, when a Riemann solver of the HLL family is employed, in order to obtain second-order accuracy the filter is switched off and both in the PPM and PLM cases, and the summation is carried over all waves, irrespective of their sign (this is further discussed in Sec.2.2.5). Finally, $S_{d,\mathrm{MHD}}$ represents the MHD source

term required in multidimensional MHD which we implement in the form (Crockett et al. 2005)

$$S_{d,\boldsymbol{i}}^{n,\mathrm{MHD}} = \begin{pmatrix} 0 \\ \frac{B_0}{\rho} \\ \vdots \\ \frac{B_{\mathbf{D}-1}}{\rho} \\ \mathbf{B} \cdot \mathbf{u} \\ u_{d_1} \\ u_{d_2} \end{pmatrix}_{\boldsymbol{i}}^{n} \left(\frac{\partial B_d}{\partial x_d} \right)_{\boldsymbol{i}}^{n} \tag{32}$$

where, as usual, $d \neq d_1 \neq d_2$ and, in this particular case, $0 \leq d_1 < d_2 < \mathbf{D}$. The normal predictor step is completed by the final corrections for a non-stiff source term according to

$$W_{\boldsymbol{i},\pm,d}^{n} = W_{\boldsymbol{i},\pm,d}^{n} + \frac{\Delta t}{2} S_{\boldsymbol{i}}^{n}. \tag{33}$$

2.2.4. CT Extended Corner Transport Upwind

After the primitive variables have been extrapolated to cell faces, we add corrections due to gradients parallel to the cell faces. We find it convenient at this point to convert back to a conservative representation, thus we operate the transformation: $W_{\boldsymbol{i},\pm,d}^{n} \leftarrow U_{\boldsymbol{i},\pm,d}^{n}$. Following the CTU scheme the corrections are expressed in terms of transverse flux gradients, with fluxes obtained from a Riemann solver, $\mathcal{R}$. In accord with the CT scheme, however, for the update of magnetic field variables we use gradients of edge-centered electric fields suitably interpolated in space and time from their face and cell centered values. Both the interpolation procedure, $\mathcal{I}_E$, and the Riemann solver, $\mathcal{R}$, will be specified at the end of this section. It suffices here to say that the time centering and interpolation accuracy of the interpolated edge-centered electric fields is consistent with that of the MHD fluxes returned by the Riemann solver.

The steps involved in the modified CTU update can then be summarized as follows:

1. Use a Riemann solver, $\mathcal{R}(U^{Left}, U^{Right})$, to obtain a first estimate of the fluxes across cell faces along each direction, d

$$F_{d,\boldsymbol{i}+\frac{1}{2}\boldsymbol{e}^d}^{1D} = \mathcal{R}(U_{\boldsymbol{i},+,d}^{n}, U_{\boldsymbol{i}+\boldsymbol{e}^d,-,d}^{n}, d). \tag{34}$$

2. Use the newly obtained fluxes with the primitive solution at time t^n to interpolate the electric fields from cell-faces and cell-centers to cell-edges

$$E_{d,\boldsymbol{i}+\frac{1}{2}\boldsymbol{e}^{d_1}+\frac{1}{2}\boldsymbol{e}^{d_2}}^{1D} = \mathcal{I}_E(F_{d_1,*+\frac{1}{2}\boldsymbol{e}^{d_1}}^{1D}, F_{d_2,*+\frac{1}{2}\boldsymbol{e}^{d_2}}^{1D}, W_*^n), \tag{35}$$

where the $*$ symbol indicates that the interpolation requires values of the arguments at various cell centers and faces.

3. As part of the CTU prescription to obtain $(1, 1, 1)$ diagonal coupling, apply corrections to density, momentum and energy components of $U_{i,\pm,d_1}$, due to one set of transverse flux derivatives along d_2. For each face d_1, there will be $\mathbf{D} - 1$ such corrected states, one for each direction perpendicular to d_1. The corrected states read

$$U^n_{i,\pm,d_1,d_2} = U^n_{i,\pm,d_1} - \frac{\Delta t}{3\Delta x}(F^{1D}_{d_2,i+\frac{1}{2}e^{d_2}} - F^{1D}_{d_2,i-\frac{1}{2}e^{d_2}}). \tag{36}$$

4. Likewise, use the CT scheme to correct magnetic field components affected by the same set of transverse flux derivatives. There are $\mathbf{D} - 1$ magnetic field components of $U^n_{i,\pm,d_1}$ on the face d_1 which are affected by the transverse flux along d_2. First, the component along d_1, which we indicate with $U_{B_{d_1}}$, is corrected as

$$U^n_{B_{d_1},i\pm,d_1,d_2} = U^n_{B_{d_1},i\pm,d_1} - \varepsilon_{d_1 d_3 d_2} \frac{\Delta t}{3\Delta x}\left(E^{1D}_{d_3,i\pm\frac{1}{2}e^{d_1}+\frac{1}{2}e^{d_2}} - E^{1D}_{d_3,i\pm\frac{1}{2}e^{d_1}-\frac{1}{2}e^{d_2}}\right). \tag{37}$$

Second, we correct the magnetic field component, $U_{B_{d_3}}$, parallel to the cell face and directed along the remaining direction $d_3 \neq d_2 \neq d_1$. As in Gardiner & Stone (2008), for this component we average the contributions from the faces at $i+\frac{1}{2}e^{d_3}$ and $i-\frac{1}{2}e^{d_3}$, obtaining

$$U^n_{B_{d_3},i\pm,d_1,d_2} = U^n_{B_{d_3},i\pm,d_1} - \varepsilon_{d_1 d_3 d_2} \frac{\Delta t}{6\Delta x}\left[\left(E^{1D}_{d_1,i+\frac{1}{2}e^{d_3}+\frac{1}{2}e^{d_2}} - E^{1D}_{d_1,i+\frac{1}{2}e^{d_3}-\frac{1}{2}e^{d_2}}\right)\right.$$
$$\left. + \left(E^{1D}_{d_1,i-\frac{1}{2}e^{d_3}+\frac{1}{2}e^{d_2}} - E^{1D}_{d_1,i-\frac{1}{2}e^{d_3}-\frac{1}{2}e^{d_2}}\right)\right]. \tag{38}$$

5. Use a Riemann solver to obtain fluxes for each pair of states corrected for transverse fluxes. This provides $\mathbf{D} - 1$ fluxes per cell face.

$$F_{d_1,i+\frac{1}{2}e^{d_1},d_2} = \mathcal{R}(U_{i,+,d_1,d_2}, U_{i+e^{d_1},-,d_1,d_2}, d_1) \tag{39}$$

$$d_1 \neq d_2, \ 0 \leq d_1, d_2 < \mathbf{D}$$

6. Obtain new interpolated values of the electric field from the averages of the above computed fluxes

$$E_{d,i+\frac{1}{2}e^{d_1}+\frac{1}{2}e^{d_2}} = \mathcal{I}_E(\tilde{F}_{d_1,*+\frac{1}{2}e^{d_1}}, \tilde{F}_{d_2,*+\frac{1}{2}e^{d_2}}, W^n_*) \tag{40}$$

where

$$\tilde{F}_{d_1,i+\frac{1}{2}e^{d_1}} = \frac{1}{2}(F_{d_1,i+\frac{1}{2}e^{d_1},d_2} + F_{d_1,i+\frac{1}{2}e^{d_1},d_3}) \tag{41}$$

$$\tilde{F}_{d_2,i+\frac{1}{2}e^{d_2}} = \frac{1}{2}(F_{d_2,i+\frac{1}{2}e^{d_2},d_1} + F_{d_2,i+\frac{1}{2}e^{d_2},d_3}). \tag{42}$$

7. Compute final corrections to the density, momentum and energy components of $U_{i,\pm,d}$ due to transverse fluxes using the above Riemann solutions, according to

$$
\begin{aligned}
U_{i,\pm,d}^{n+\frac{1}{2}} = U_{i,\pm,d} \ &- \ \frac{\Delta t}{2\Delta x}(F_{d_1,i+\frac{1}{2}e^{d_1},d_2} - F_{d_1,i-\frac{1}{2}e^{d_1},d_2}) \\
&- \ \frac{\Delta t}{2\Delta x}(F_{d_2,i+\frac{1}{2}e^{d_2},d_1} - F_{d_2,i-\frac{1}{2}e^{d_2},d_1}) \\
&d \neq d_1 \neq d_2, \ 0 \leq d, d_1, d_2 < \mathbf{D}
\end{aligned} \tag{43}
$$

8. Likewise, use the CT scheme to apply final corrections to magnetic field components. In analogy to Eq. (37) in step 4 we write

$$
\begin{aligned}
U_{B_d,i,\pm,d}^{n+\frac{1}{2}} = U_{B_d,i,\pm,d}^{n} - \varepsilon_{dd_1d_2}\frac{\Delta t}{2\Delta x}\Big[&\Big(E_{d_1,i\pm\frac{1}{2}e^{d}+\frac{1}{2}e^{d_2}} - E_{d_1,i\pm\frac{1}{2}e^{d}-\frac{1}{2}e^{d_2}}\Big) \\
&- \Big(E_{d_2,i\pm\frac{1}{2}e^{d}+\frac{1}{2}e^{d_1}} - E_{d_2,i\pm\frac{1}{2}e^{d}-\frac{1}{2}e^{d_1}}\Big)\Big]
\end{aligned} \tag{44}
$$

Finally, in analogy to Eq. (38) the magnetic field components parallel to the cell face are updated according to the CT scheme as

$$
\begin{aligned}
U_{B_{d_1},i\pm,d}^{n+\frac{1}{2}} = U_{B_{d_1},i\pm,d}^{n} - \varepsilon_{dd_1d_2}\frac{\Delta t}{2\Delta x}\Big[&\Big(E_{d,i+\frac{1}{2}e^{d_1}+\frac{1}{2}e^{d_2}} - E_{d,i+\frac{1}{2}e^{d_1}-\frac{1}{2}e^{d_2}}\Big) \\
&+ \Big(E_{d,i-\frac{1}{2}e^{d_1}+\frac{1}{2}e^{d_2}} - E_{d,i-\frac{1}{2}e^{d_1}-\frac{1}{2}e^{d_2}}\Big) \\
&- \Big(E_{d_2,i+\frac{1}{2}e^{d_1}+\frac{1}{2}e^{d}} - E_{d_2,i+\frac{1}{2}e^{d_1}-\frac{1}{2}e^{d}}\Big) \\
&- \Big(E_{d_2,i-\frac{1}{2}e^{d_1}+\frac{1}{2}e^{d}} - E_{d_2,i-\frac{1}{2}e^{d_1}-\frac{1}{2}e^{d}}\Big)\Big].
\end{aligned} \tag{45}
$$

9. Compute final second-order estimate of time averaged fluxes

$$
F_{d,i+\frac{1}{2}e^{d}}^{n+\frac{1}{2}} = \mathcal{R}(U_{i,+,d}^{n+\frac{1}{2}}, U_{i+e^{d},-,d}^{n+\frac{1}{2}}, d). \tag{46}
$$

10. Compute final estimate of the electric field using the above fluxes and an updated value for the cell-centered conservative variables using the averaged fluxes in Eq. (41), namely

$$
E_{d,i+\frac{1}{2}e^{d_1}+\frac{1}{2}e^{d_2}}^{n+\frac{1}{2}} = \mathcal{I}_E(F_{d_1,*+\frac{1}{2}e^{d_1}}^{n+\frac{1}{2}}, F_{d_2,*+\frac{1}{2}e^{d_2}}^{n+\frac{1}{2}}, \tilde{W}_*^n), \tag{47}
$$

where

$$
\tilde{W}_i^n = W_i^n - \frac{1}{2}\frac{\Delta t}{\Delta x}\nabla_U W \cdot \sum_{d=0}^{\mathbf{D}-1}\Big(\tilde{F}_{d,i+\frac{1}{2}e^{d}} - \tilde{F}_{d,i-\frac{1}{2}e^{d}}\Big).
$$

and the operator $\nabla_U W$ symbolizes the transformation from conservative to primitive variables.

11. Finally update cell-centered conservative variables using Eq. (13) with the fluxes in (46) and the face-centered magnetic field variables using Eq. (17) with the electric field in (47) and synchronize the magnetic variables using Eq. (19).

2.2.5. Riemann Solver

For the purpose of this paper, we have implemented the HLLD solver recently developed by Miyoshi & Kusano (2005). This is an extended version of the original HLL solver for the MHD, which includes the entropy, Alfvén and fast magnetosonic waves. The solver appears quite accurate and robust and relatively inexpensive. As already pointed out in order for the fluxes returned by HLL-type solvers to be second-order accurate, the projector P is modified in such a way that the summation is carried over all waves, irrespective of their sign. This is because the fluxes returned by these solvers are built on the spatially reconstructed solutions on the left and right hand sides of the cell interfaces. The solver is extensively documented in the original paper and its description will not be repeated here.

2.2.6. Interpolation Scheme for the Edge-Centered Electric Field

In this section we describe the scheme used to interpolate the face-centered electric fields returned by the Riemann solver onto cell edges. In Sec. 2.2.4 this was indicated with the notation, $\mathcal{I}_E$. It is important for the stability of the overall algorithm to choose this interpolation scheme in such a way that there is consistency between the time-update of the face-centered magnetic field, the cell-centered variables and the synchronization step of the magnetic variables, Eq. (19). For this purpose we have adopted the upwind scheme described in Gardiner & Stone (2005, 2008). This will be described next, for the case of three dimensions. In this case each cell edge is shared by four adjacent faces from which the electric field can be interpolated. Hence, these four interpolated values will be arithmetically averaged. The scheme for $\mathcal{I}_E()$ uses three arguments,

$$E_{d,\boldsymbol{i}+\frac{1}{2}\boldsymbol{e}^{d_1}+\frac{1}{2}\boldsymbol{e}^{d_2}} = \mathcal{I}_E(F_{d_1,*+\frac{1}{2}\boldsymbol{e}^{d_1}}, F_{d_2,*+\frac{1}{2}\boldsymbol{e}^{d_2}}, W_*),$$

where the $*$ symbol indicates that the interpolation requires values of the arguments at different cells and faces. The face-centered fluxes define the face-centered electric fields according to Eq. (15), and the cell-centered primitive state variable, $W_{\boldsymbol{i}}$, is used to define a cell-centered electric field according to the usual formula

$$E_{d,\boldsymbol{i}} = -\varepsilon_{dd_1d_2}(u_{d_1,\boldsymbol{i}}B_{d_2,\boldsymbol{i}} - u_{d_2,\boldsymbol{i}}B_{d_1,\boldsymbol{i}}),$$

with the velocity and magnetic field variables given by the components of W_i. The cell-centered electric field is used together with face-centered electric fields (15) to define the following transverse quasi-cell-centered gradients

$$\left(\frac{\delta E_d}{\delta x_{d_1}}\right)_{i+\frac{1}{4}e^{d_1}} = 2\frac{E_{d,i+\frac{1}{2}e^{d_1}} - E_{d,i}}{\Delta x}. \tag{48}$$

In turn, these gradients are used to define quasi-face-centered gradients of the electric field by the upwind scheme (Gardiner & Stone 2005)

$$\left(\frac{\delta E_d}{\delta x_{d_2}}\right)_{i+\frac{1}{2}e^{d_1}+\frac{1}{4}e^{d_2}} = \begin{cases} \left(\frac{\delta E_d}{\delta x_{d_2}}\right)_{i+\frac{1}{4}e^{d_2}} & \text{if } u_{i+\frac{1}{2}e^{d_2}} > 0 \\ \left(\frac{\delta E_d}{\delta x_{d_2}}\right)_{i+\frac{3}{4}e^{d_2}} & \text{if } u_{i+\frac{1}{2}e^{d_2}} < 0 \\ \frac{1}{2}\left[\left(\frac{\delta E_d}{\delta x_{d_2}}\right)_{i+\frac{1}{4}e^{d_2}} + \left(\frac{\delta E_d}{\delta x_{d_2}}\right)_{i+\frac{3}{4}e^{d_2}}\right] & \text{otherwise.} \end{cases}$$

With the above definitions, the interpolated edge-centered electric field is defined as

$$\begin{aligned} E_{d,i+\frac{1}{2}e^{d_1}+\frac{1}{2}e^{d_2}} = \quad & \frac{1}{4} \left(E_{d,i+\frac{1}{2}e^{d_1}} + E_{d,i+e^{d_2}+\frac{1}{2}e^{d_1}} + E_{d,i+\frac{1}{2}e^{d_2}} + E_{d,i+e^{d_1}+\frac{1}{2}e^{d_2}}\right) \\ + \quad & \frac{\Delta x}{8} \left[\left(\frac{\delta E_d}{\delta x_{d_2}}\right)_{i+\frac{1}{2}e^{d_1}+\frac{1}{4}e^{d_2}} - \left(\frac{\delta E_d}{\delta x_{d_2}}\right)_{i+\frac{1}{2}e^{d_1}+\frac{3}{4}e^{d_2}}\right] \\ + \quad & \frac{\Delta x}{8} \left[\left(\frac{\delta E_d}{\delta x_{d_1}}\right)_{i+\frac{1}{2}e^{d_2}+\frac{1}{4}e^{d_1}} - \left(\frac{\delta E_d}{\delta x_{d_1}}\right)_{i+\frac{1}{2}e^{d_2}+\frac{3}{4}e^{d_1}}\right]. \end{aligned} \tag{49}$$

3. Tests

3.1. Convergence Rates in Smooth Flows

In this section we test the correctness of our implementation by measuring the convergence rate of the numerical solution returned by the code. The test is based on the propagation of Alfvén, fast and slow MHD waves. The waves have small amplitude, $\delta = 10^{-5}$, so that we expect to observe the nominal second order convergence rate predicted by numerical analysis.

In the following tests the initial conditions are provided for the primitive variables by defining the unperturbed state, W, and the superposed perturbation, δW, corresponding to the wave. The size of the computational box is, $L = 1$, the geometry is one- or two-dimensional and the boundary conditions are periodic. The adiabatic index is $\gamma = 5/3$. While we have experimented with different choices of orientation of the wave-vector with

respect to the grid, namely $\mathbf{k}/2\pi = (1,0),\ (0,1),\ (1/\sqrt{2}, 1/\sqrt{2}),\ (2/\sqrt{5}, 1/\sqrt{5})$, we find the same convergence rates in all cases. Thus, we simply report the results for the few representative tests listed in Table 1.

In order to measure the rate at which the numerical solution converges, for each problem we carry out a set of 5 simulation runs employing $N_{cell} = 16, 32, 64, 128, 256$ for a total range of 16. For each run the time-step size is fixed, scales inversely with N_{cell}, and corresponds roughly to a CFL number 0.8. The convergence rate is measured using Richardson extrapolation. Given the numerical solution q_r at resolution r we first estimate the error at a given point (i, j), as

$$\varepsilon_{r;i,j} = q_r(i,j) - \bar{q}_{r+1}(i,j), \tag{50}$$

where $\bar{q}_{r+1}$ is the solution at the next finer resolution, spatially averaged onto the coarser grid. We then take the n-norm of the error

$$L_n = \|\varepsilon_r\|_n = \left(\sum |\varepsilon_{r;i,j}|^n v_{i,j} \right)^{1/n}, \tag{51}$$

where, $v_{i,j} = \Delta x^2$ is the cell volume, and estimate the convergence rate as

$$R_n = \frac{\ln[L_n(\varepsilon_r)/L_n(\varepsilon_s)]}{\ln(\Delta x_r/\Delta x_s)}. \tag{52}$$

For each case listed in Table 1, we produce a corresponding Table 2-4 reporting the L_1, L_2 and L_∞ norms of the error and the corresponding convergence rates, R_1, R_2 and R_∞, as defined above.

Table 1: Run Set

run	δ	$\mathbf{k}/2\pi$	Type
A	10^{-5}	$(1,0)$	Alfvén
B	10^{-5}	$(2/\sqrt{5}, 1/\sqrt{5})$	Alfvén
C	10^{-5}	$(1,0)$	Fast
D	10^{-5}	$(2/\sqrt{5}, 1/\sqrt{5})$	Fast
E	10^{-5}	$(1,0)$	Slow
F	10^{-5}	$(2/\sqrt{5}, 1/\sqrt{5})$	Slow

3.1.1. Alfvén Waves

The test based on the propagation of the Alfvén wave is characterized by the following unperturbed state and superposed perturbation (Crockett et al. 2005)

$$
W = \begin{pmatrix} \rho_0 \\ u_x \\ u_y \\ u_z \\ P_0 \\ B_0/\sqrt{2} \\ B_0/\sqrt{2} \\ 0 \end{pmatrix}, \qquad \delta W = \begin{pmatrix} 0 \\ 0 \\ 0 \\ -c_A \\ 0 \\ 0 \\ 0 \\ B_0 \end{pmatrix} \delta \sin(\mathbf{k} \cdot \mathbf{x}) \tag{53}
$$

where $\rho_0 = P_0 = B_0 = 1$ and $u_x = u_y = u_z = 0$, $c_A = B_0/\sqrt{\rho_0} = 1$, is the Alfvén speed, and $\mathbf{k}$ and $\mathbf{x}$ are the wavevector and position vector respectively. The convergence rates for the perturbed quantities are summarized in Table 2. In both tests, with different $\mathbf{k}$, both the $z-$components of the velocity and magnetic field converge with second-order accuracy. The error on the unperturbed variables (not reported) is much smaller and converges at the same rate as the perturbed variables until dominated by the machine round-off error. As already pointed out, tests with different orientation of $\mathbf{k}$ show the same convergence rates.

3.1.2. Fast and Slow Magnetosonic Waves

For fast and slow magnetosonic waves the unperturbed state and the superposed perturbations read (Crockett et al. 2005)

$$
W = \begin{pmatrix} \rho_0 \\ u_x \\ u_y \\ u_z \\ P_0 \\ B_0 \hat{b}_x \\ B_0 \hat{b}_y \\ 0 \end{pmatrix}, \qquad \delta W = \begin{pmatrix} \rho_0 \\ (\sqrt{2}c_w^2 \hat{b}_y - c_g^2 \hat{k}_y)/c_w \\ -(\sqrt{2}c_w^2 \hat{b}_x - c_g^2 \hat{k}_x)/c_w \\ 0 \\ \rho_0 c_g^2 \\ -\sqrt{2}B_0(c_w^2 - c_g^2)\hat{k}_y/c_A^2 \\ \sqrt{2}B_0(c_w^2 - c_g^2)\hat{k}_x/c_A^2 \\ 0 \end{pmatrix} \delta \sin(\mathbf{k} \cdot \mathbf{x}) \tag{54}
$$

where, $\hat{b}$ is the unit vector along the magnetic field vector and is at $\pi/4$ radians with respect to the unit vector $\hat{k} \equiv \mathbf{k}/k$, $c_g = \sqrt{\gamma P_0/\rho_0}$ is the gas sound speed, c_w is the speed of fast

or slow MHD waves and all other symbols take the meaning and values as in the previous section.

The convergence rates are reported in Table 3 and 4 for fast and slow waves, respectively. As with Alfvén waves, the errors in the perturbed variables converge with second order accuracy, while the error in the unperturbed variables are much smaller and converge at the same rate until they are affected by machine precision.

3.2. Riemann Problem

We next consider a set of Riemann problems from the literature which are standard tests for MHD algorithms. The Riemann problem is described in general by the following initial-value problem

$$W[x_0, t = 0] = \begin{cases} W_{left} & \text{if} \quad x_0 \leq 0.5 \\ W_{right} & \text{if} \quad x_0 > 0.5 \end{cases} \tag{55}$$

where $W_{left/right}$ represents the primitive variables to the left/right of the initial discontinuity. The set of problems and corresponding initial conditions are summarized in Table 5, except for the value of the $x-$component of the magnetic field which will be specified for each problem explicitly. In all cases we use a CFL number $C_{\text{CFL}} = 0.8$, third order PPM reconstruction scheme and characteristic limiting. The domain size is $L = 1$ and the boundary conditions are simply, $W(x_0 = 0, t) = W_{left}$, and, $W(x_0 = 1, t) = W_{right}$.

We should point out that Miyoshi & Kusano (2005) have carried out extensive tests of their HLLD solver, which we employ in our code, particularly to compare its performance with that of Roe and other solvers of the HLLC family. We shall repeat some of those tests here. Note that while in most cases Miyoshi & Kusano (2005) used a first order accurate piece-wise constant reconstruction scheme, we have used the third order accurate PPM method, so the solution profiles in our plots appear sharper. The tests which we will perform below involve the full set of MHD waves, including those associated with the slow mode which is not included explicitly in the HLLD solver. However, in accord with Miyoshi & Kusano (2005), we find that in these tests the full MHD structure of the solution, including features associated with the slow mode, is correctly reproduced.

3.2.1. Brio & Wu

We begin with the Riemann problem presented in Brio & Wu (1988), listed at the top of Table 5. The $x-$component of the magnetic field is $B_x = 0.75$ and the adiabatic index $\gamma = 2$
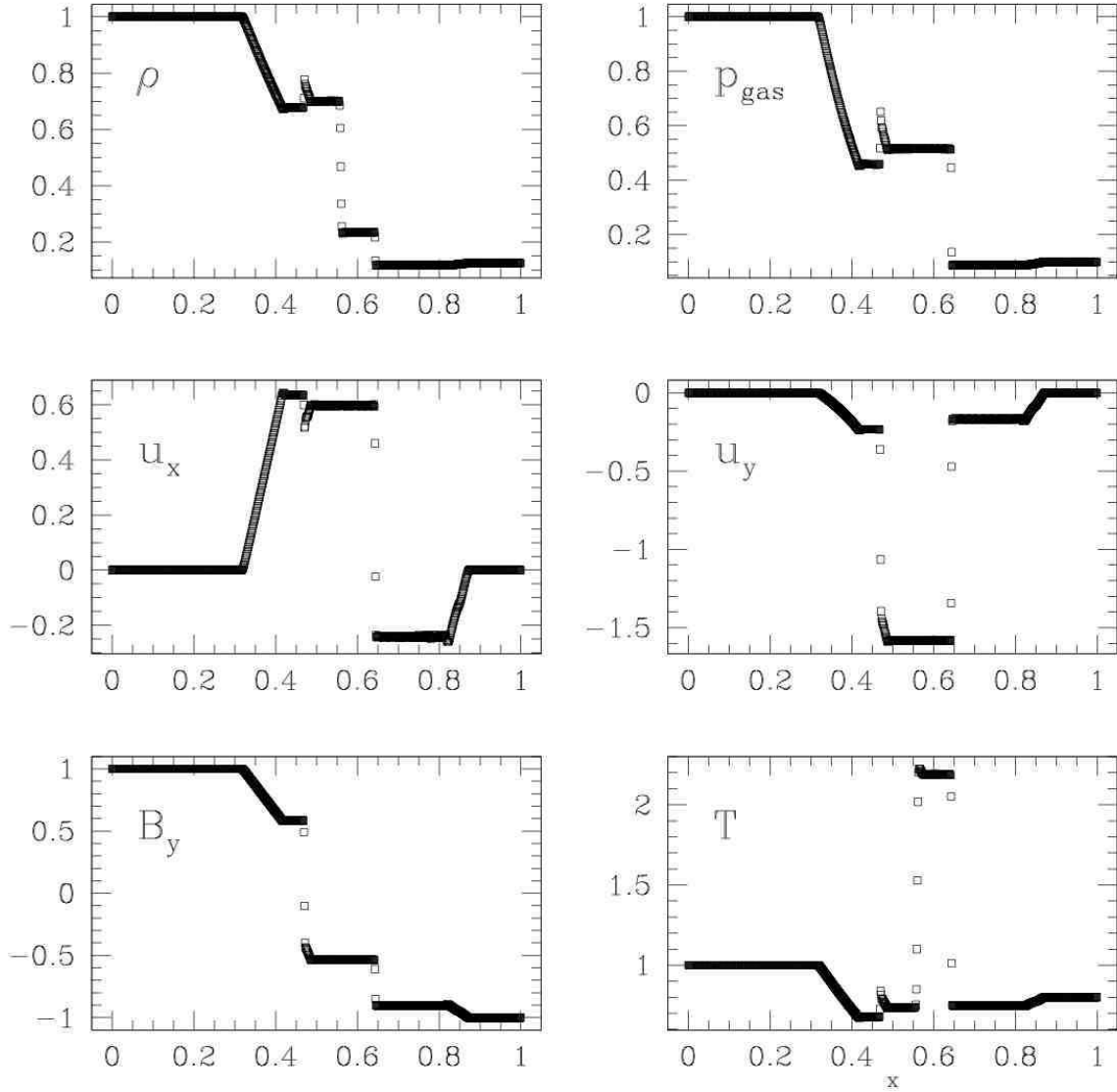
Fig. 2.— Brio & Wu shock tube problem: solution for $t = 0.1$ solved on a grid using 800 zones. See Table 5 for the initial conditions. From left to right and top to bottom shown are, respectively: density, pressure, velocity components along the x and y axis, magnetic field component along the $y-$axis and temperature.

as in the original paper. Following common practice, the problem is solved on a grid with 800 points along the x−axis and the solution is computed until time $t = 0.1$. The results are shown in Fig. 2. All the solution features are well reproduced, including, from left to right, a fast rarefaction followed by a slow compound wave, moving to the left, and a contact discontinuity, slow shock and fast rarefaction moving to the right (Brio & Wu 1988). As usual with shock-capturing methods, shocks are resolved with a couple of zones throughout the duration of the calculation, while the contact discontinuities, captured here within a few zones, tend to spread out over time. There are some oscillations in the x−component of the velocity field. These are not present if we adopt a PLM reconstruction scheme, but worsen if we switch from a characteristic to a primitive limiting scheme.

3.2.2. Dai & Woodward

The second Riemann problem listed in table 5 is taken from Dai & Woodward (1998). In this case the x−component of the magnetic field is $B_x = 4/\sqrt{4\pi}$ and the adiabatic index $\gamma = 5/3$. The problem is solved on a grid with 512 points along the x−axis and the solution is computed until time $t = 0.2$. The results are shown in Fig. 3. The initial conditions for this problem expose the full eigenstructure of the MHD system, as they produce three pairs of MHD waves traveling in opposite directions with respect to the initial discontinuity, in addition to the contact wave. The waves include fast and slow shocks responsible, among others, for the jumps in the pressure and velocity fields, the contact wave which appears in the density field alone, and the rotational discontinuity which affects the magnetic field components alone. As in the previous case, while all discontinuities are well reproduced, shocks are the sharpest features captured with about two zones.

3.2.3. Ryu & Jones

The third Riemann problem in our table 5 is one of the many problems studied by Ryu & Jones (1995). Here $B_x = 0.7$ and $\gamma = 5/3$. The problem is solved on a grid with 512 points along the x−axis and the solution is computed until time $t = 0.16$, as in the original paper. The results are shown in Fig. 4. The solution to this problem includes, from left to right, a hydrodynamic rarefaction, a switch-on slow shock, a contact discontinuity, a slow shock, a rotational discontinuity and a fast rarefaction. Switch-on/off fast/slow shocks are interesting MHD solutions that cause the tangential magnetic field to turn on/off, respectively. As in the previous tests the structure of the solution is well reproduced, including the features associated with the slow MHD mode, and the discontinuities are captured within a few to
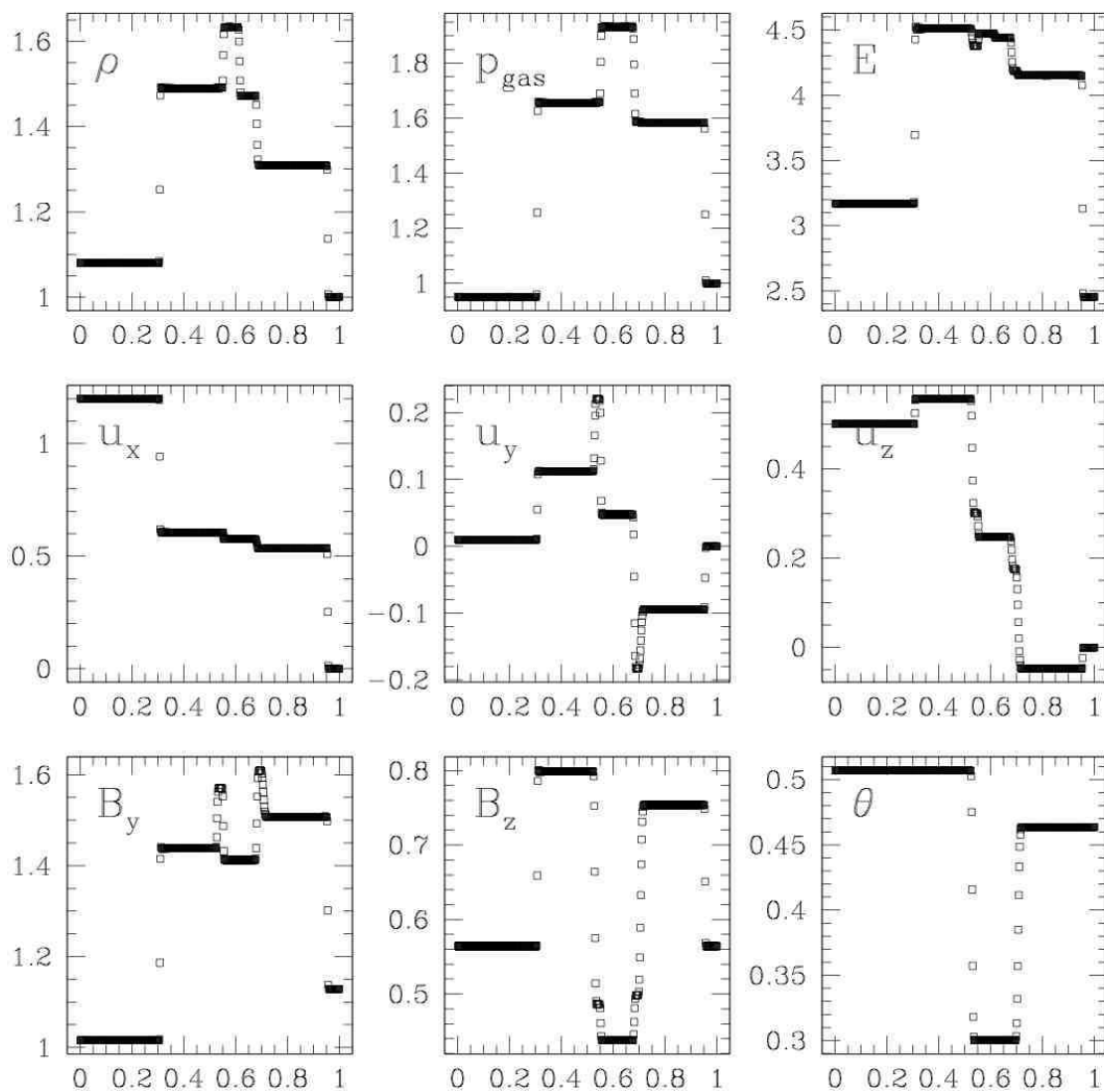
Fig. 3.— Dai & Woodward shock tube problem: solution for $t = 0.2$ solved on a grid using 512 zones. See Table 5 for the initial conditions. From left to right and top to bottom, shown are, respectively: density, pressure, energy, three velocity components magnetic field components, along the y and z axis, and $\theta = \tan^{-1}(B_z/By)$.
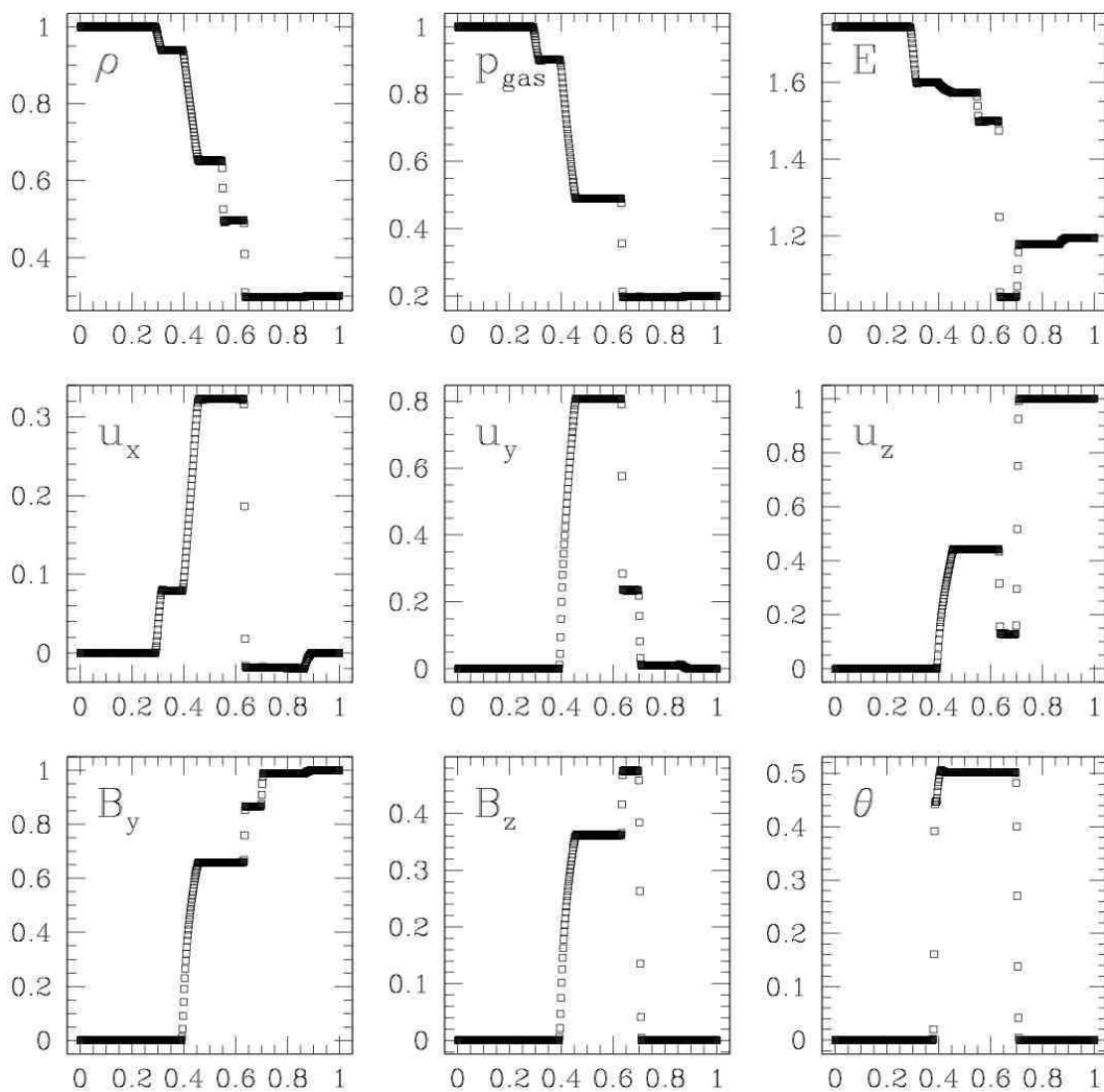
Fig. 4.— Ryu & Jones shock tube problem: solution for $t = 0.16$ solved on a grid using 512 zones. See Table 5 for the initial conditions. From left to right and top to bottom, shown are, respectively: density, pressure, energy, three velocity components, magnetic field components along the y and z axis, and $\theta = \tan^{-1}(B_z/By)$.

several zones.

3.2.4. Fast rarefaction

The last one-dimensional Riemann problem listed in table 5 is similar to the ones presented in Einfeldt et al. (1991). Its purpose is to test the method/code robustness in the case of flows in which the energy is dominated by the kinetic component and unphysical states with negative density or internal energy can arise. This problem is solved using a grid with 256 grid points. The solution at time $t = 0.1$ is shown in Fig. 5. The results in Fig. 5 show a stable solution which correctly reproduces the two rarefaction waves propagating away from the grid midpoint. A very similar test has also been performed by Stone et al. (2008), with similar results, and Miyoshi & Kusano (2005). The latter authors actually use a faster expansion velocity, namely $u_{x,\frac{L}{R}} = \mp 3$, in their initial conditions and show that when used with a (first order) Godunov's method the numerical solution remains stable. While we are able to reproduce their result we find that at high resolution some spurious oscillations can be generated when a higher-order Godunov's method is used. This may suggest the need for artificial viscosity in the case of highly supersonic expansions with higher-order Godunov's methods.

3.2.5. Inclined Dai & Woodward Shock-Tube Problem

We have repeated the problem in Sec. 3.2.2 with the initial discontinuity inclined with respect to the grid such that its normal has components $\vec{n} = (2,1)/\sqrt{5}$. This problem tests the ability of the code to reproduce one-dimensional solutions when they are not aligned with the grid. Besides the numerical tests, there are a few other complications related with the numerical set-up of this problem. First, the boundary conditions need revision. To avoid the implementation of "shift-periodic" boundary conditions (Tóth 2000), we use a domain with size $(2L, L)\,2/\sqrt{5}$. This allows us to accommodate two adjacent identical problems along the direction, $\vec{n} = (2,1)/\sqrt{5}$, and apply periodic boundary conditions to the domain. [1] In addition, since the magnetic field rotates across the discontinuity, the initialization is non-trivial and, unless a special precaution is taken, e.g. by deriving the magnetic field

---

[1] Obviously, since the sequence of states will be $W_{left}, W_{right}, W_{left}, W_{right}$, the interaction at the second interface will produce a similar Riemann problem with inverted initial conditions. However, we will present only part of the solution, selected for proper comparison with the analogous one-dimensional problem in Sec. 3.2.2.
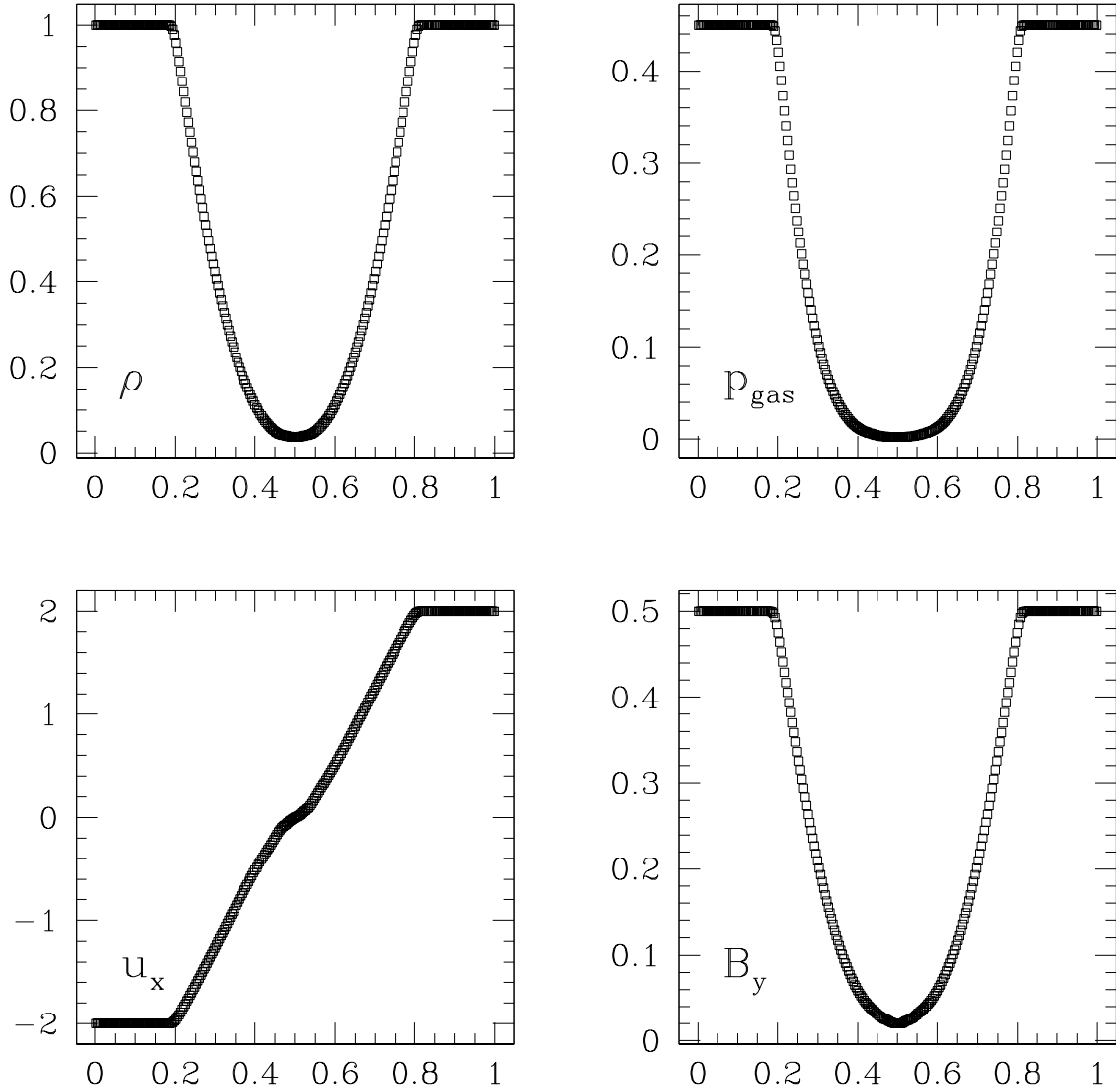
Fig. 5.— Fast rarefaction: solution for $t = 0.16$ solved on a grid using 512 zones. See Table 5 for the initial conditions. From left to right and top to bottom, shown are, respectively: density, gas pressure, $x-$component of the velocity and $y-$component of the magnetic field.
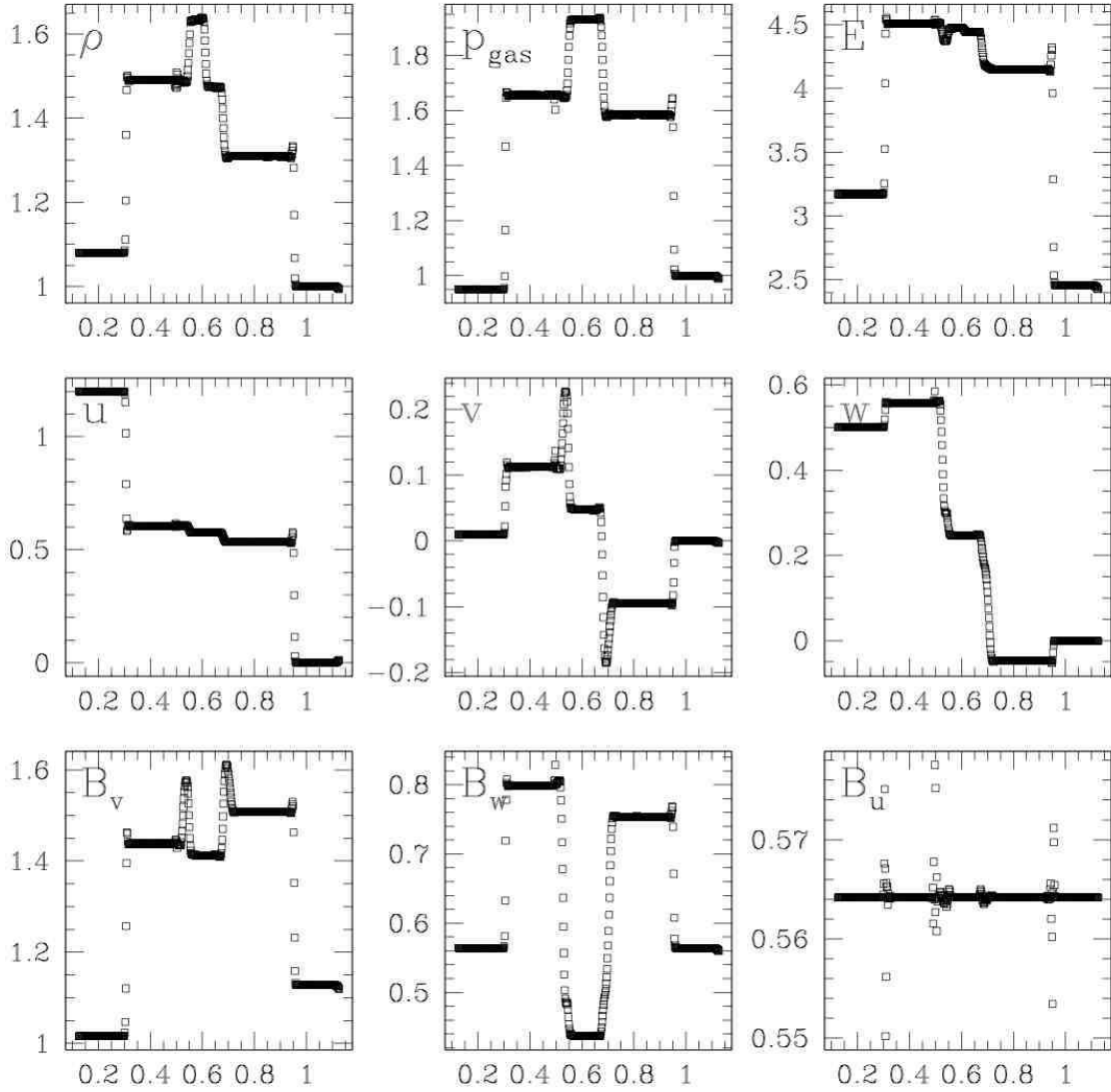
Fig. 6.— Inclined version of Dai & Woodward shock tube problem: solution for $t = 0.2$ solved on a grid using 512 zones. See Table 5 for the initial conditions. From left to right and top to bottom, shown are, respectively: density, pressure, energy, three velocity components and three magnetic field components.

from a vector potential, the initial magnetic field will not be divergence-free (this is not an issue in the special case in which $\vec{n}$ is along the diagonal and there is symmetry among the coordinate axis). In our case no such precaution is taken and we just remap the initial conditions onto the rotated grid. As a result there is a jump in the normal component of the magnetic field across the discontinuity. This causes some minor artifacts with respect to the one-dimensional solution. This is acceptable since we are interested in making sure that the structure of the one-dimensional solution is reproduced with fidelity and the waves propagate at the correct speed.

In order to solve the problem, we have covered the domain with a grid of 1144×572 cells. This corresponds to 512 cells along the direction perpendicular to $\vec{n}$, which is equivalent to the resolution used in Sec. 3.2.2. The results are shown in Fig. 6 where we plot the values of the solution along the first row of the computational domain, starting from $\frac{1}{2}L + \delta_L$ to $\frac{3}{2}L + \delta_L$. The starting point is shifted by $\delta_L \sim 0.2$ to the left, to hide the perturbation of W_{left} due to the interaction with the state to its left (which is W_{right}). The vectorial components (u, v, w) are the equivalent of (x, y, z) in the rotated system.

Fig. 6 shows that the one-dimensional solution is correctly recovered when the plane of the discontinuity is inclined with respect to the grid. We notice some oscillation at the fast magnetosonic shocks, which to some extent are also present in Fig. 7 of Gardiner & Stone (2008). These are probably associated with the oscillations in the normal component of the magnetic field, also reported in the last panel of Fig. 6. These can perhaps be suppressed with more aggressive limiters (Londrillo & del Zanna 2004). There is also a spurious feature, ahead of the left-moving rotational discontinuity, which is probably due to the non-solenoidal character of the initial magnetic field. However, none of these features affect either the jump conditions or the wave speeds, as attested to by the very good correspondence between the solution in Fig. 6 and the one-dimensional counterpart in Fig. 3.

3.3.   Magnetic Loop Advection

In this section we test the ability of the code to follow the advection of a loop of weak magnetic field frozen in a background flow. This problem is non-trivial for conservative schemes and Gardiner & Stone (2005, 2008) emphasize that spurious results will be produced as a result of improper account of the MHD source terms entering the predictor step, as discussed in Sec. 2.2.3. The initial conditions are detailed in Gardiner & Stone (2008). The loop is basically a tube of magnetic flux frozen in a medium with unit density and pressure, $\rho = p_{gas} = 1$ and uniform advection velocity, $\mathbf{u}_{loop}$, to be specified below.

We carry out the test both in a 2D or a 3D geometry. For the 2D case, we align the loop axis with the x_2 coordinate axis of the computational domain. The vector potential from which the magnetic field is initialized is then given by, $\mathbf{A} = (0, 0, A_2)$, with

$$A_2 = \begin{cases} B_0(R - r) & \text{if} \quad r \leq R, \\ 0 & \text{if} \quad r > R, \end{cases} \tag{56}$$

where $B_0 = 10^{-3}$, $r = \sqrt{x_0^2 + x_1^2}$, and, $R = 0.3$, is the radius of the tube. The computational domain itself consists of a rectangular box of dimensions $(2N, N)$ with periodic boundaries, and the loop advection velocity is $\mathbf{u}_{loop} = (2, 1)$.

For the 3D configuration, the axis of the tube is tilted around the x_1 axis by $\theta = \arctan 2$ radians (clockwise) and the tube is advected with velocity $\mathbf{u}_{loop} = (1, 1, 2)$. The domain is still periodic but has dimensions $(N, N, 2N)$. The vector potential is still defined as in (56) but with respect to the new coordinates

$$\begin{aligned} x_0' &= x_0 \cos \theta + x_2 \sin \theta, \\ x_1' &= x_1, \\ x_2' &= -x_0 \sin \theta + x_2 \cos \theta. \end{aligned} \tag{57}$$

The results of this test are first illustrated in Figures 7 and 8 which show the magnetic pressure at $t = 2$ for the 2D and 3D cases respectively. In the former case $N = 64$, while in the latter case $N = 128$. The results are comparable to other MHD implementations, in particular Gardiner & Stone (2005, 2008). As pointed out by those authors, the magnetic pressure suffers dissipation mostly close to the loop center (where the curl of $\vec{B}$ is singular) and boundary. However, both in the 2D and 3D cases, the loop retains to a good extent its initial symmetry and energy. This latter point is further illustrated in Fig. 9, reporting the evolution of the normalized magnetic pressure up to $t = 2$ for three different resolutions. One important aspect of the 3D version of this test is to check the ability of the scheme to keep the magnetic field component along the loop axis, B_3, close to zero. This is important here because we have not strictly followed the recommendation of Gardiner & Stone (2008) when implementing the MHD source terms in the predictor step. The evolution of B_3 is reported in Figure 10, again for three different values of the resolution, up to $t = 2$. Due to the simpler form of the employed MHD source terms, $\langle |B_3| \rangle$ is larger than found in Gardiner & Stone (2008) at the same time ($t = 1$), but only slightly so and B_3 remains negligible compared to the total magnetic field.
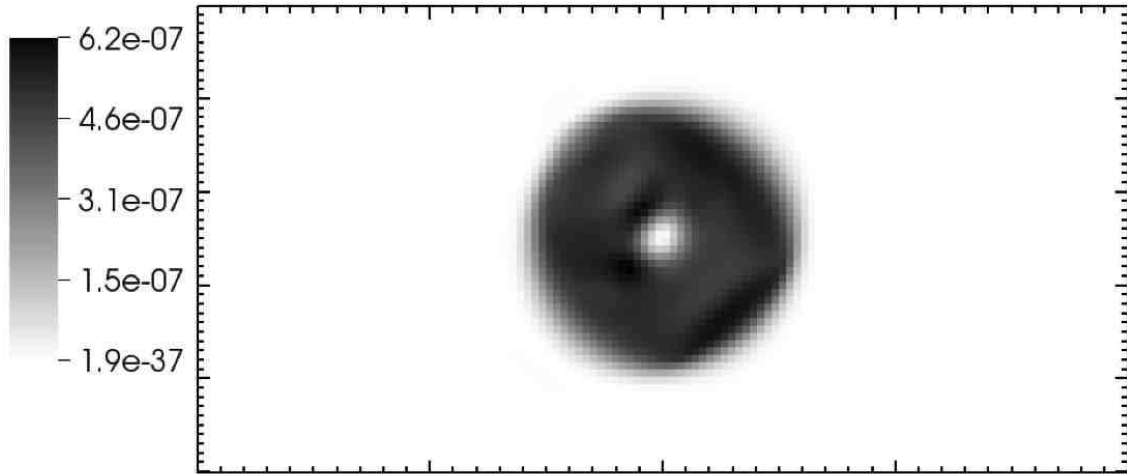
Fig. 7.— Loop advection in 2D: magnetic pressure at $t = 2$ from a calculation using $N = 64$, and corresponding colorbar (top left).

Table 2: Convergence Rates for Alfvén Waves.

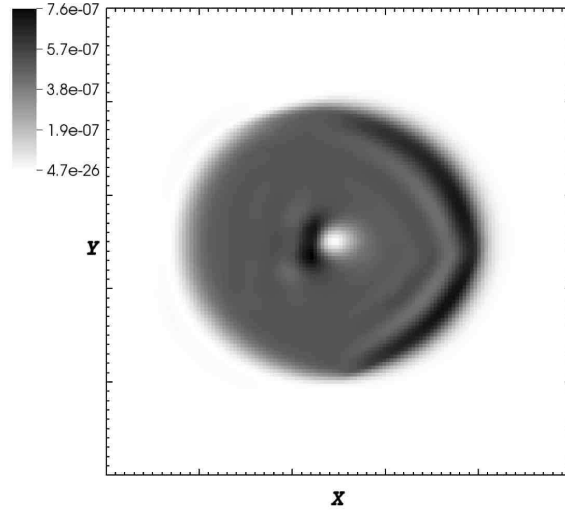| N_{cells}	L_1	R_1	L_2	R_2	L_∞	R_∞	L_1	R_1	L_2	R_2	L_∞	R_∞
				Case A: $\delta = 10^{-5}$, $\mathbf{k} = 2\pi(1,0)$								
	$z-$**velocity**						$z-$**magnetic**					
16	7.5E-09	–	1.7E-08	–	4.7E-08	–	7.5E-09	–	1.7E-08	–	4.7E-08	–
32	1.9E-09	2.0	4.2E-09	2.0	1.2E-08	2.0	1.9E-09	2.0	4.2E-09	2.0	1.2E-08	2.0
64	4.8E-10	2.0	1.1E-09	2.0	3.0E-09	2.0	4.8E-10	2.0	1.1E-09	2.0	3.0E-09	2.0
128	1.2E-10	2.0	2.7E-10	2.0	7.5E-10	2.0	1.2E-10	2.0	2.7E-10	2.0	7.5E-10	2.0
				Case B: $\delta = 10^{-5}$, $\mathbf{k} = 2\pi(2,1)/\sqrt{5}$								
	$z-$**velocity**						$z-$**magnetic**					
16	7.6E-08	–	1.2E-07	–	2.4E-07	–	7.8E-08	–	1.2E-07	–	2.3E-07	–
32	2.0E-08	1.9	3.1E-08	2.0	6.2E-08	1.9	2.0E-08	2.0	3.1E-08	2.0	6.2E-08	1.9
64	4.9E-09	2.0	7.8E-09	2.0	1.5E-08	2.0	5.0E-09	2.0	7.8E-09	2.0	1.6E-08	2.0
128	1.2E-09	2.0	1.9E-09	2.0	4.0E-09	2.0	1.2E-09	2.0	2.0E-09	2.0	4.0E-09	2.0

Fig. 8.— Loop advection in 3D: cut of the magnetic pressure at $z = 0.5$ of the magnetic pressure at $t = 2$ from a calculation using $N = 128$, and corresponding colorbar (top left).

Table 3: Convergence Rates for Fast MHD Waves.

N_{cells}	L_1	R_1	L_2	R_2	L_∞	R_∞	L_1	R_1	L_2	R_2	L_∞	R_∞
						Case C: $\delta = 10^{-5}$, $\mathbf{k} = 2\pi(1,0)$					
	density-gas						$x-$**vel-gas**					
16	7.5E-09	–	1.7E-08	–	4.6E-08	–	1.1E-08	–	2.4E-08	–	6.6E-08	–
32	1.9E-09	2.0	4.2E-09	2.0	1.2E-08	2.0	2.7E-09	2.0	6.0E-09	2.0	1.7E-08	2.0
64	4.8E-10	2.0	1.1E-09	2.0	3.0E-09	2.0	6.8E-10	2.0	1.5E-09	2.0	4.3E-09	2.0
128	1.2E-10	2.0	2.7E-10	2.0	7.5E-10	2.0	1.7E-10	2.0	3.8E-10	2.0	1.1E-09	2.0
	$y-$**vel-gas**						**pressure**					
16	3.4E-09	–	7.6E-09	–	2.1E-08	–	1.0E-08	–	2.3E-08	–	6.5E-08	–
32	8.7E-10	2.0	1.9E-09	2.0	5.5E-09	2.0	2.7E-09	2.0	5.9E-09	2.0	1.7E-08	2.0
64	2.2E-10	2.0	4.9E-10	2.0	1.4E-09	2.0	6.7E-10	2.0	1.5E-09	2.0	4.2E-09	2.0
128	5.5E-11	2.0	1.2E-10	2.0	3.5E-10	2.0	1.7E-10	2.0	3.7E-10	2.0	1.1E-09	2.0
	$y-$**magnetic**											
16	7.0E-09	–	1.5E-08	–	4.3E-08	–						
32	1.8E-09	2.0	3.9E-09	2.0	1.1E-08	2.0						
64	4.4E-10	2.0	9.9E-10	2.0	2.8E-09	2.0						
128	1.1E-10	2.0	2.5E-10	2.0	7.0E-10	2.0						
						Case D: $\delta = 10^{-5}$, $\mathbf{k} = 2\pi(2,1)/\sqrt{5}$					
	density-gas						$x-$**vel-gas**					
16	7.7E-08	–	1.2E-07	–	2.4E-07	–	9.2E-08	–	1.4E-07	–	2.9E-07	–
32	2.1E-08	1.8	3.4E-08	1.8	6.8E-08	1.8	2.6E-08	1.8	4.1E-08	1.8	8.2E-08	1.9
64	5.6E-09	1.9	8.7E-09	1.9	1.7E-08	2.0	6.7E-09	1.9	1.1E-08	1.9	2.1E-08	1.9
128	1.4E-09	2.0	2.2E-09	2.0	4.4E-09	2.0	1.7E-09	2.0	2.7E-09	2.0	5.4E-09	2.0
	$y-$**vel-gas**						**pressure**					
16	2.3E-08	–	3.7E-08	–	7.8E-08	–	1.0E-07	–	1.6E-07	–	3.5E-07	–
32	5.6E-09	2.0	8.8E-09	2.1	1.7E-08	2.2	3.0E-08	1.8	4.7E-08	1.8	9.7E-08	1.9
64	1.3E-09	2.1	2.1E-09	2.1	4.1E-09	2.1	7.8E-09	1.9	1.2E-08	1.9	2.5E-08	2.0
128	3.2E-10	2.1	5.0E-10	2.1	1.0E-09	2.0	2.0E-09	2.0	3.1E-09	2.0	6.2E-09	2.0
	$x-$**magnetic**						$y-$**magnetic**					
16	3.9E-08	–	6.3E-08	–	1.6E-07	–	4.7E-08	–	8.2E-08	–	1.9E-07	–
32	9.0E-09	2.1	1.4E-08	2.2	3.3E-08	2.3	1.2E-08	2.0	1.9E-08	2.1	4.4E-08	2.1
64	2.1E-09	2.1	3.3E-09	2.1	7.3E-09	2.2	2.9E-09	2.0	4.6E-09	2.1	1.0E-08	2.1
128	5.2E-10	2.0	8.1E-10	2.0	1.7E-09	2.1	7.3E-10	2.0	1.1E-09	2.0	2.4E-09	2.1

Table 4: Convergence Rates Slow MHD Waves.

| N_{cells}	L_1	R_1	L_2	R_2	L_∞	R_∞	L_1	R_1	L_2	R_2	L_∞	R_∞
				Case E: $\delta = 10^{-5}$, $\mathbf{k} = 2\pi(1,0)$								
	density-gas						$x-$**vel-gas**					
16	7.5E-09	–	1.7E-08	–	4.7E-08	–	4.4E-09	–	9.9E-09	–	2.8E-08	–
32	1.9E-09	2.0	4.2E-09	2.0	1.2E-08	2.0	1.1E-09	2.0	2.5E-09	2.0	7.0E-09	2.0
64	4.8E-10	2.0	1.1E-09	2.0	3.0E-09	2.0	2.8E-10	2.0	6.2E-10	2.0	1.8E-09	2.0
128	1.2E-10	2.0	2.7E-10	2.0	7.5E-10	2.0	7.0E-11	2.0	1.6E-10	2.0	4.4E-10	2.0
	$y-$**vel-gas**						**pressure**					
16	1.4E-08	–	3.1E-08	–	8.7E-08	–	1.1E-08	–	2.3E-08	–	6.6E-08	–
32	3.5E-09	2.0	7.7E-09	2.0	2.2E-08	2.0	2.7E-09	2.0	5.9E-09	2.0	1.7E-08	2.0
64	8.7E-10	2.0	1.9E-09	2.0	5.5E-09	2.0	6.7E-10	2.0	1.5E-09	2.0	4.2E-09	2.0
128	2.2E-10	2.0	4.8E-10	2.0	1.4E-09	2.0	1.7E-10	2.0	3.7E-10	2.0	1.1E-09	2.0
	$y-$**magnetic**											
16	1.1E-08	–	2.5E-08	–	7.1E-08	–						
32	2.9E-09	2.0	6.4E-09	2.0	1.8E-08	2.0						
64	7.2E-10	2.0	1.6E-09	2.0	4.5E-09	2.0						
128	1.8E-10	2.0	4.0E-10	2.0	1.1E-09	2.0						
				Case F: $\delta = 10^{-5}$, $\mathbf{k} = 2\pi(2,1)/\sqrt{5}$								
	densit$y-$**gas**						$x-$**vel-gas**					
16	6.1E-08	–	9.5E-08	–	1.9E-07	–	5.7E-08	–	8.9E-08	–	1.8E-07	–
32	1.6E-08	2.0	2.4E-08	2.0	4.9E-08	2.0	1.4E-08	2.0	2.3E-08	2.0	4.7E-08	1.9
64	3.9E-09	2.0	6.2E-09	2.0	1.2E-08	2.0	3.7E-09	2.0	5.8E-09	2.0	1.2E-08	2.0
128	9.9E-10	2.0	1.6E-09	2.0	3.1E-09	2.0	9.2E-10	2.0	1.4E-09	2.0	2.9E-09	2.0
	$y-$**vel-gas**						**pressure**					
16	1.4E-07	–	2.2E-07	–	4.4E-07	–	8.5E-08	–	1.3E-07	–	2.8E-07	–
32	3.6E-08	2.0	5.7E-08	2.0	1.1E-07	1.9	2.2E-08	2.0	3.5E-08	2.0	7.0E-08	2.0
64	9.1E-09	2.0	1.4E-08	2.0	2.9E-08	2.0	5.6E-09	2.0	8.7E-09	2.0	1.8E-08	2.0
128	2.3E-09	2.0	3.6E-09	2.0	7.2E-09	2.0	1.4E-09	2.0	2.2E-09	2.0	4.4E-09	2.0
	$x-$**magnetic**						$y-$**magnetic**					
16	6.1E-08	–	9.6E-08	–	2.0E-07	–	6.3E-08	–	9.9E-08	–	2.2E-07	–
32	1.5E-08	2.0	2.4E-08	2.0	5.0E-08	2.0	1.6E-08	1.9	2.6E-08	1.9	5.5E-08	2.0
64	3.9E-09	2.0	6.1E-09	2.0	1.2E-08	2.0	4.1E-09	2.0	6.5E-09	2.0	1.3E-08	2.0
128	9.8E-10	2.0	1.5E-09	2.0	3.1E-09	2.0	1.0E-09	2.0	1.6E-09	2.0	3.3E-09	2.0
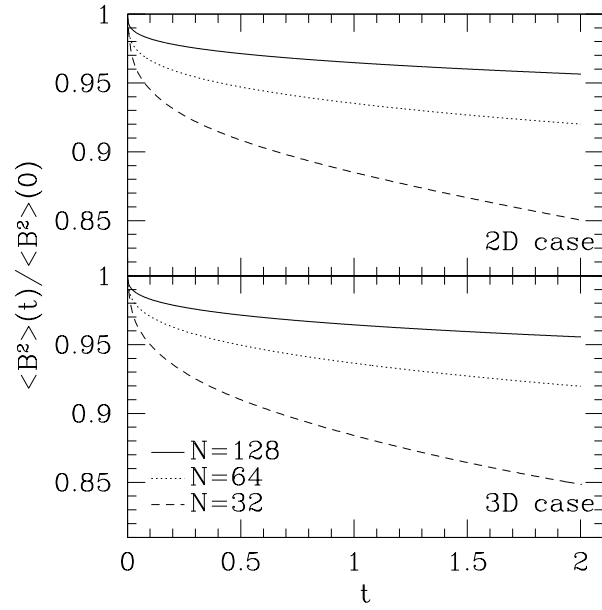
Fig. 9.— Loop advection: time evolution of the magnetic energy for the 2D (top) and 3D (bottom) cases, for three different resolutions.
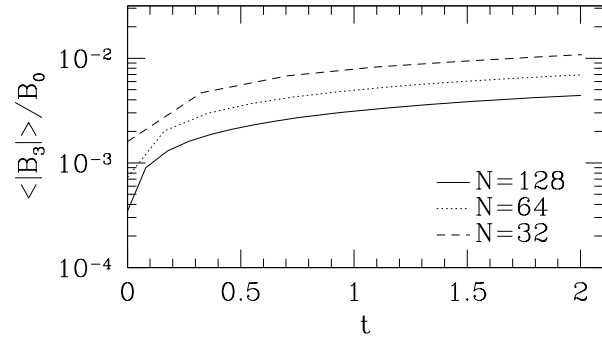

Fig. 10.— Loop advection in 3D: time evolution of B_3, the magnetic field component aligned with the loop axis, for three different resolutions.

Table 5: Riemann Problem Set

Test	left-state							right-state						
	ρ	u_x	u_y	u_z	p	B_y	B_z	ρ	u_x	u_y	u_z	p	B_y	B_z
Brio-Wu	1	0	0	0	1	1	0	0.128	0	0	0	0.1	-1	0
Dai-Woodward	1.08	1.2	0.01	0.5	0.95	$\frac{3.6}{\sqrt{4\pi}}$	$\frac{2}{\sqrt{4\pi}}$	1	0	0	0	1	$\frac{4}{\sqrt{4\pi}}$	$\frac{2}{\sqrt{4\pi}}$
Ryu-Jones	1	0	0	0	1	0	0	0.3	0	0	1	0.2	1	0
Fast Raref.	1	-2	0	0	0.45	0.5	0	1	2	0	0	0.45	0.5	0

3.4.   Orszag-Tang Vortex

We now turn to a series of classical multidimensional tests for MHD codes. First, we compute the compressible Orszag-Tang vortex problem (Orszag & Tang 1979). We solve this problem on a computational domain of size $L = 1$ with periodic boundary conditions and a rectangular grid of 200×200 cells. We use an adiabatic index $\gamma = 5/3$. We present results obtained using the PPM reconstruction scheme and primitive limiting, but very similar results are produced using characteristic limiting. The initial conditions in terms of the primitive variables are as follows

$$W = [\rho_0, -u_0 \sin(2\pi y), u_0 \sin(2\pi x), 0, P_0, -B_0 \sin(2\pi y), B_0 \sin(4\pi x), 0]^T \qquad (58)$$

where $\rho_0 = 25/36\pi$, $P_0 = 5/12\pi$ and u_0 and B_0 are defined in terms of the sonic Mach number, $\mathcal{M} = 1$, and plasma beta, $\beta = 10/3$, respectively. Although the initial conditions are smooth, eventually the flow develops a complex structure with sharp features and discontinuities. In Fig. 11 we show the contours of the numerical solution for density, gas pressure, kinetic energy and magnetic pressure at time $t = 0.5$. One dimensional cuts along the line $y = 0.4277$ for the thermal pressure (top) and magnetic pressure (bottom) are also shown in Fig. 12. The code maintains the symmetry of the solution with respect to the central point. In addition, Fig. 12 shows that discontinuous features are captured within a few zones. Finally, the solution can be compared with similar plots at the same solution time produced by other authors (e.g. Ryu et al. 1998; Tóth 2000; Stone et al. 2008), from which it appears that the code produces the correct flow structures.

3.5.   Rotor Problem

Another two-dimensional problem commonly used as a test for multidimensional MHD codes is the *rotor* problem described in Balsara & Spicer (1999). It consists of a rotating disk of dense material, threaded by a magnetic field initially directed along the $x-$axis, and
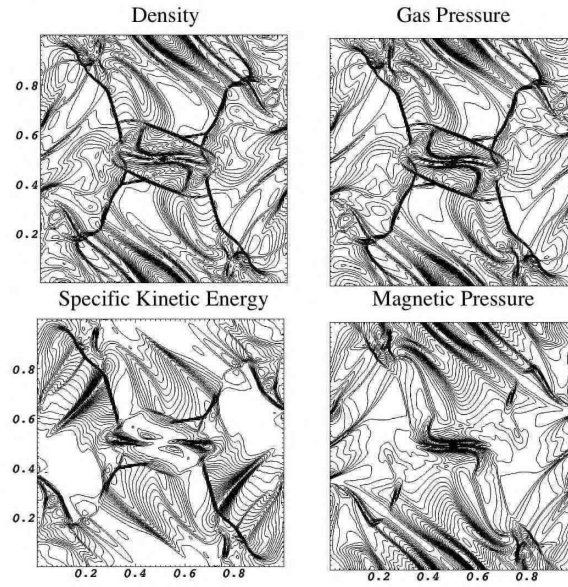
Fig. 11.— Orszag-Tang Vortex: thirty equally-spaced contour levels between max and min value of the numerical solution at $t = 0.5$ respectively for density (top-left), gas pressure (top-right), specific kinetic energy (bottom-left) and magnetic pressure (bottom-right).
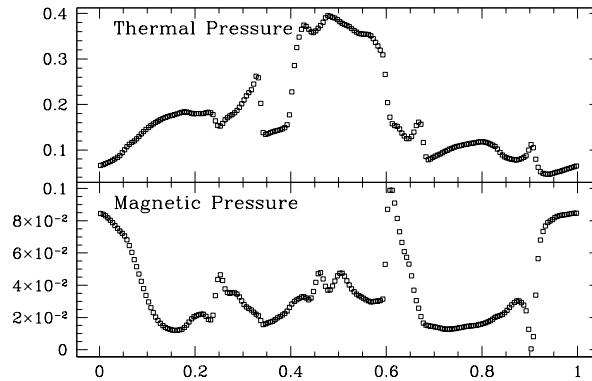

Fig. 12.— Orszag-Tang Vortex: One-dimensional cuts along the $x-$axis at $y = 0.4277$ for the thermal pressure (top) and magnetic pressure (bottom).

embedded in a tenuous ambient medium at rest. As the rotor spins, it winds up the magnetic field lines, generating Alfvén waves which propagate into the ambient medium. The problem is solved on a computational domain of size $L = 1$ with periodic boundary conditions and covered with a rectangular grid of 400×400 cells. The adiabatic index is $\gamma = 1.4$. We use the PPM reconstruction scheme and primitive limiting, although the use of characteristic limiting produces very similar results. The setup of the initial conditions corresponds to the first rotor problem discussed in Tóth (2000), i.e.

$$W[x, t = 0] = \begin{cases} W_{disk} & \text{if} \quad r < r_{disk}, \\ W_{amb} & \text{if} \quad r > r_{amb}, \end{cases} \tag{59}$$

where $W_{disk} = [\rho_{disk}, -\frac{u_0}{r_0}(y-0.5), \frac{u_0}{r_0}(x-0.5), 0, P_0, B_0, 0, 0]^T$, $W_{amb} = (\rho_0, 0, 0, 0, P_0, B_0, 0, 0)^T$, $r \equiv \sqrt{x^2 + y^2}$, r_{disk} defines the disk radius and r_{amb} delimits the ambient medium. In the transition region between the ambient medium and the rotor the density and velocity fields are interpolated according to $\rho = (\rho_{disk} - \rho_0)f(r) + \rho_0$, $u_x = -f(r)u_0(y - 0.5)/r$ and $u_y = f(r)u_0(x - 0.5)/r$, with $f(r) = (r_{amb} - r)/(r_{amb} - r_{disk})$, whereas density and pressure remain uniform. The results for this test are presented in Fig. 13, which effectively reproduces Fig. 18 of Tóth (2000). The numerical solution appears very well behaved and the code seem to pass this test as well.

4. Extension to Adaptive Mesh Refinement

Following Berger & Colella (1989) and Balsara (2001), we employ block-structured local refinement to increase the computational resolution where the accuracy of the solution needs to be improved. Our implementation is basically an extension of the MHD case of Miniati & Colella (2007a).

Generalizing the case discussed in Sec. 2.1.1, the problem domain is discretized on a hierarchy of grids, $\Gamma^0 \ldots \Gamma^{\ell_{max}}$, each with its own spacing h^ℓ and refinement ratio $n_{ref}^\ell \equiv h^\ell/h^{\ell+1}$. We assume that refinement ratio is always even.

Calculations are performed on a hierarchy of meshes $\{\Omega^\ell\}_{\ell=0}^{\ell=\ell_{max}}$ such that for each ℓ, $\Omega^\ell \subset \Gamma^\ell$. The base-level uniform rectangular mesh spans the domain, so $\Omega^0 = \Gamma^0$. Cells for which improved resolution is desired are marked for refinement, grouped together into logically rectangular regions, and refined by a factor of n_{ref}^0 to create the level 1 domain Ω^1. Further refinement levels, Ω^ℓ, may then be created as needed in the same way starting from a refinement level $\Omega^{\ell-1}$, with refinement ratio $n_{ref}^{\ell-1}$. The set of generated meshes Ω^ℓ is assumed to be properly nested, meaning that (a) any control volume $i^l \in \Omega^\ell$ is either completely covered by $(n_{ref}^\ell)^{\mathbf{D}}$ finer control volumes or by none, and (b) for any given pair

of meshes $\Omega^{\ell-1}$ and $\Omega^{\ell+1}$ there is always a layer of cells of Ω^ℓ separating the two. By analogy with the single grid case we can construct the set $\Omega_f^{\ell;e^d}$ corresponding to the faces in Ω^ℓ, and likewise the set $\Omega_e^{\ell;e^d}$ for the corresponding edges. Similarly, for each level, we can define a divergence and curl operators for face and edge centered vectors, respectively.

The part of an AMR level which is "covered" by refinement is denoted as the *covered region*, while the *valid region* of a given level ℓ is the part of Ω^ℓ not covered by refinement. For computational convenience, solution values are maintained in covered regions as well as valid regions, but only the solution in valid regions is considered to be valid. The *composite solution* spans the computational domain and is the union of the valid-region solutions on each level. The coarse-fine interface between levels ℓ and $\ell - 1$ is denoted by $\partial\Omega^\ell$.

As in Berger & Colella (1989), we refine in time as well as space, with $\Delta t^{\ell+1} = \Delta t^\ell / n_{ref}^\ell$. The update of the solution on the hierarchy of AMR levels can be described recursively as the update of a single AMR level ℓ from time t^ℓ to time $t^\ell + \Delta t^\ell$ (Fig. 4).

Extending the CT scheme described in this paper requires some additions to the standard set of algorithmic tools generally used for fully cell-centered discretizations of hyperbolic conservation laws like that in Berger & Colella (1989). Most of the additional algorithmic pieces result from the addition of the solenoidal face-centered $\vec{B}$ field.

4.1. Filling Ghost cells

Before each single level update from time t^ℓ to time $t^\ell + \Delta t^\ell$, a ring of "ghost" cells sufficiently large to complete the stencils required to update valid-region data on each grid-patch is filled in. For the scheme described here, we require 6 and 4 ghost cells for PPM and PLM reconstruction methods, respectively. Where possible, ghost values are filled by copying valid-region data from other grids on the same level ℓ or possibly by a discrete representation of physical domain boundary conditions. Where neither of these is possible, values must be interpolated from the coarser level $\ell-1$ solution. Cell-centered quantities are interpolated using a limited piecewise-linear scheme. The face-centered $\vec{B}$ field is likewise interpolated using a piecewise-linear scheme as follows:

1. First, $\vec{B}^{\ell-1}$ is linearly interpolated in time to t^ℓ. (Recall that level $\ell - 1$ has already been updated from $t^{\ell-1}$ to $(t^{\ell-1} + \Delta t^{\ell-1})$, and $t^{\ell-1} \leq t^\ell < (t^{\ell-1} + \Delta t^{\ell-1})$.)

2. Then, fine-level faces which overlie coarse-mesh faces are filled using piecewise linear interpolation of co-planar coarse-mesh faces.

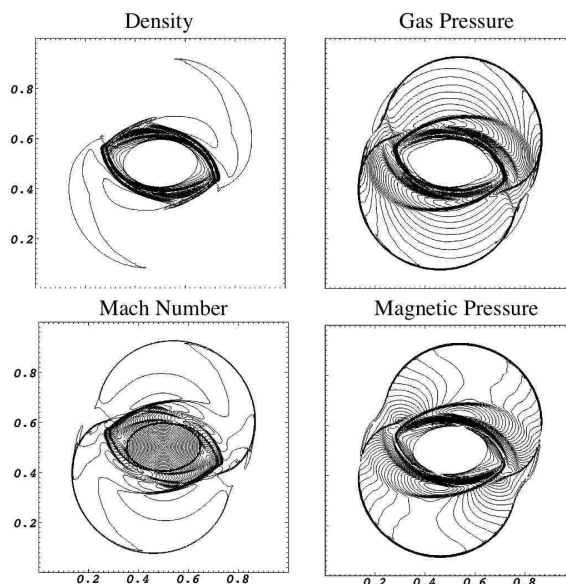3. Finally, values for fine-level faces which do not overlie coarse-mesh faces are linearly

Fig. 13.— Rotor Problem: thirty equally-spaced contour levels between max and min value of the numerical solution at $t = 0.15$ respectively for density (top-left), gas pressure (top-right), Mach number (bottom-left) and magnetic pressure (bottom-right).

LevelAdvance($\ell, t^\ell, \Delta t^\ell$)

    SingleLevelUpdate($\ell, t^\ell, \Delta t^\ell$):

        Interpolate solution values as needed from next coarser level ($\ell - 1$)

        Update solution on level ℓ using scheme described in Section 2.2

        if ($\ell < \ell_{\max}$): increment fine flux registers

        if ($\ell > 0$): increment coarser-level flux registers

        $t^\ell := t^\ell + \Delta t^\ell$

    Recursively update any finer levels:

        if ($\ell < \ell_{\max}$) **then**

            $\Delta t^{\ell+1} = \frac{\Delta t^\ell}{n_{ref}^\ell}$

            for $n = 1, n_{ref}^{ell}$

                LevelAdvance($\ell + 1, t^{\ell+1}, \Delta t^{\ell+1}$)

            end for

            "Synchronize" levels ℓ and level $\ell + 1$

        end if

end LevelAdvance

Fig. 14.— Recursive AMR timestep

interpolated between the two surrounding co-directional faces for which there are already values (either fine-level faces on the coarse-fine boundary or fine-level values interpolated in step (1)).

Note that we have not found it necessary to use a divergence-free interpolation scheme like that described in Balsara (2001) to fill in values for ghost faces.

4.2.   Synchronization

After the sub-cycled advance of level $\ell + 1$, the solutions on levels ℓ and $\ell + 1$ have reached the same solution time ($t^\ell = t^{\ell+1}$), and are then *synchronized*. For cell-centered conserved variables, synchronization is identical to that used in Berger & Colella (1989):

1. Replace level ℓ solution with the averaged level $\ell + 1$ solution in covered regions.

2. Because the fluxes used to update the fine-level solution were computed independently of those used to compute coarse-level updates, conservation will not be maintained at coarse-fine interfaces. In Berger & Colella (1989) and Martin & Colella (2000), *flux registers* are defined along the coarse-fine interface between levels ℓ and $\ell+1$, in which the fluxes used to compute coarse- and fine-level updates are stored. Since we consider the fine-level fluxes to be more accurate, we update the solution in the coarse cells adjoining the coarse-fine interface with the "reflux-divergence" of the difference of the fluxes:

$$U^\ell := U^\ell - \Delta t^\ell D_R^\ell (\sum_{n=1}^{n_{ref}^\ell} \langle F^{\ell+1} \rangle - F^\ell) \tag{60}$$

where U^ℓ is the vector of conserved quantities, D_R is the "reflux divergence" operator, F^ℓ is the vector of fluxes used to update U^ℓ, $\langle F^{\ell+1} \rangle$ is the average of the level $(\ell + 1)$ fluxes on the underlying level ℓ faces, and the sum is over sub-cycled $\ell + 1$ timesteps.

Synchronization for the face-centered magnetic field looks similar, and takes the same form as described in Balsara (2001):

1. Replace level ℓ magnetic field $\vec{B}^\ell$ with the averaged level $\ell+1$ solution on covered faces.

2. Because the edge-centered electric fields on each level are computed independently, the composite $\vec{B}$ field will no longer be solenoidal. We treat this using an analogue to the face-centered flux registers used for cell-centered data, as presented in Balsara

(2001). We store the edge-centered electric fields along coarse-fine interfaces, then increment the coarse-level magnetic field at faces bordering the coarse-fine interface with a *reflux-curl* operator applied to the coarse-fine mismatch in the edge-centered electric fields.

4.3. Regridding

It is often desirable for refined regions to periodically adapt as the solution evolves in time. When newly refined regions are created, cell-centered fields are also interpolated from coarse-level data using limited piecewise-linear interpolation. For $\vec{B}$ field values of newly refined faces, we use the divergence-free interpolation scheme described in Balsara (2001). The scheme is defined for refinement ratios $n_{ref} = 2$, but it can be applied recursively for larger values of the refinement ratio.

4.4. Shock-Cloud Interaction

As an example of an AMR-MHD application we compute the interaction of a cloud with a strong shock wave. This process is common in the interstellar medium where shocks produced by supernova explosions interact with the surrounding multi-phase medium (Klein et al. 1994; Mac Low et al. 1994). Related processes, characterized by similar hydrodynamic structures, are the supersonic motion of an over-dense cloud through a thin magnetized medium (Schiano et al. 1995; Jones et al. 1996; Vietri et al. 1997; Miniati et al. 1999b; Gregori et al. 1999, 2000), or supersonic clouds collisions (Lattanzio et al. 1985; Klein et al. 1995; Miniati et al. 1997, 1999a).

The initial conditions for our problem are as follows: the background gas has unit density and thermal pressure, and is at rest; a cloud with the same pressure but 10 times higher density, moves through the thin gas with a velocity $v_c = -3.47871373$ along the x direction. A plane-parallel shock with Mach number $\mathcal{M} = 10$ propagates along the same axis but in the opposite direction to the cloud. The initial magnetic field is uniform, of unit strength and aligned with the $x-$axis. The computational box has dimensions $[0, 1] \times [0, 0.5] \times [0, 0.5]$. The boundary conditions correspond to supersonic inflow and outflow for the lower and upper boundaries of the $x-$axis, and are periodic otherwise. The calculation is carried out in three dimensions on a base grid of $64 \times 32 \times 32$ cells. Two additional levels of refinement, with refinement ratio 4, are generated dynamically in regions where the normalized undivided density gradient $|\Delta \rho|/\rho > 0.1$, and/or in the presence of shocks according to the criteria

$|\Delta P|/P > 0.1$ and $\nabla \cdot \mathbf{v} < 0$.

Fig. 15 shows from top to bottom the solution for the density, gas pressure, magnetic field magnitude and plasma beta parameter ($\beta = P_{gas}/P_B$), at time $t = 0.021251$, corresponding to 160 cycles on the finest level. The main features, discussed at length in the above papers, are correctly reproduced. The plane shock front moving from the left crushes the cloud. As the cloud moves to the left, it creates a bow shock in front of it, where the pressure has its highest value. The cloud motion also generates a low pressure region at its rear, where the magnetic pressure dominates the gas pressure and the beta plasma is much less then unity. In addition, as the fluid flows past the cloud, the magnetic field lines entrained in the cloud body fold on themselves creating a current sheet (Jones et al. 1996).

Note that the maximum value of the normalized divergence of the magnetic field $|\Delta x \nabla \cdot \mathbf{B}|/|B|$, is a few$\times 10^{-13}$. This is completely negligible with respect to the solution value and demonstrates that our implementation of the above operators for the coarse fine magnetic field interpolation and refluxing operations is correct.

5. Extension to Cosmology

We now describe the extension of our MHD algorithm to the case of cosmological applications. This will include only a basic description of the cosmological code, for it is presented in detail elsewhere (Miniati & Colella 2007a).

For cosmological simulations it is preferable to transform away the expansion of the universe through the use of a *comoving* frame of reference. Thus we operate the transformation

$$\boldsymbol{x} \leftarrow a(t)^{-1}\,\boldsymbol{x} \tag{61}$$

from lab to comoving coordinates, where $a(t)$ is a function of time that defines the physical size of spatial scales, and $\dot{a}/a$ is the expansion rate of the universe. In addition we subtract out the velocity component due to the expansion of the universe, and retain the *peculiar* proper velocity, i.e.

$$\boldsymbol{u} \leftarrow \boldsymbol{u} - \dot{a}\,\boldsymbol{x}. \tag{62}$$

Finally, it is convenient to use *comoving* density and pressure, i.e. those expressed in terms of the comoving volume $\boldsymbol{x}^3$ as opposed to the proper volume $a^3\boldsymbol{x}^3$,

$$\rho \;\; \leftarrow a^3\,\rho, \tag{63}$$

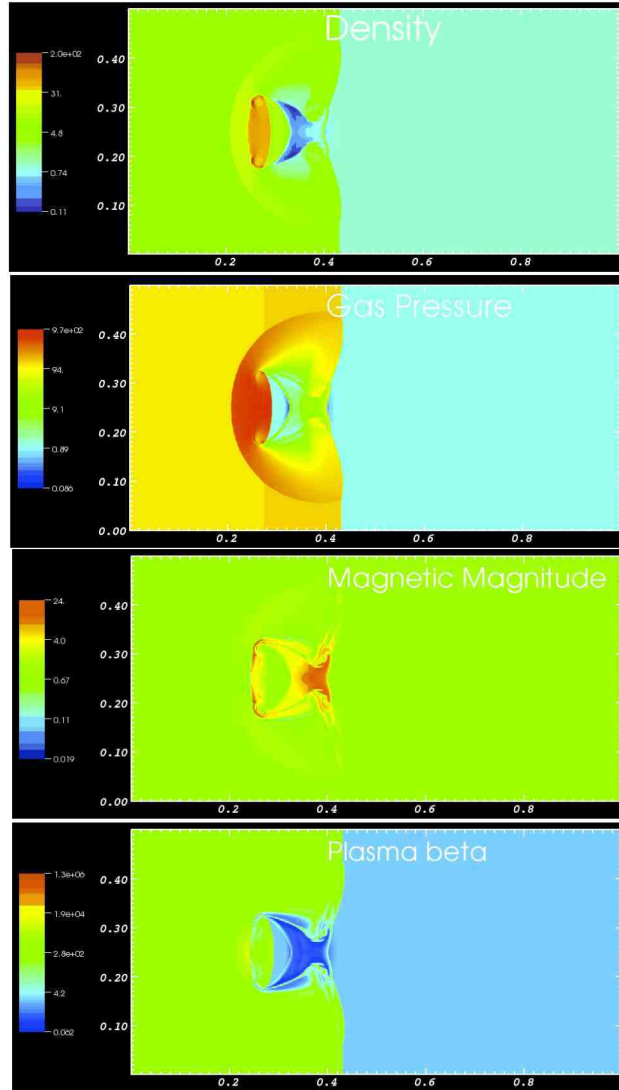$$p \;\; \leftarrow a^3\,p. \tag{64}$$

Fig. 15.— Shock-cloud interaction: from top to bottom, solution for density, gas pressure, magnetic field magnitude and plasma beta parameter, at time $t = 0.021251$.

Similarly, although the magnetic flux naturally scales with $a^2(t)$, we transform it to a pseudo-comoving variable

$$B \leftarrow a^{\frac{3}{2}} B. \tag{65}$$

The above transformations allow writing the conservation and induction equations in a form that, except for the appearance of source terms, closely resembles the original ones. This similarity allows us not only to solve for the MHD system of equations in the cosmological framework with the same algorithm described in Sec. 2 but also to apply the same menagerie of AMR tools described in Sec. 4 with virtually no modification.

In fact, in the comoving frame, $\boldsymbol{x}$, the conservation equations read

$$\frac{\partial U}{\partial t} + \frac{1}{a(t)} \nabla_{\mathbf{x}} \cdot \mathbf{F} = S, \tag{66}$$

where U and F are defined exactly as in (11) but are now expressed in terms of peculiar velocity, comoving density, comoving pressure and pseudo-comoving magnetic field. The source term on the RHS is

$$S(U) = -\frac{\dot{a}}{a} \begin{pmatrix} 0 \\ \rho u_0 \\ \vdots \\ \rho u_{\mathbf{D}-1} \\ 2\rho e - \frac{B^2}{2} \\ \frac{1}{2} B_0 \\ \vdots \\ \frac{1}{2} B_{\mathbf{D}-1} \end{pmatrix} + \rho \begin{pmatrix} 0 \\ g_0 \\ \vdots \\ g_{\mathbf{D}-1} \\ \mathbf{u} \cdot \mathbf{g} \\ 0 \\ \vdots \\ 0 \end{pmatrix}, \tag{67}$$

where the first term, $\propto \dot{a}/a$, accounts for adiabatic losses of momentum, energy, and magnetic field, and the second term, $\propto \mathbf{g}$, is due to gravity. Similarly, we rewrite Faraday's law in the comoving frame in terms of the peculiar velocity and pseudo-comoving magnetic field, i.e.

$$\frac{\partial B_d}{\partial t} = -\frac{1}{a} \frac{\partial}{\partial x_j} \left(u_j B_d - B_j u_d \right) - \frac{1}{2} \frac{\dot{a}}{a} B_d. \tag{68}$$

Based on Eq. (66) and (68) the time update of U and B is then done according to

$$U_{\boldsymbol{i}}^{n+1} = U_{\boldsymbol{i}}^n - \frac{1}{a^{n+\frac{1}{2}}} \frac{\Delta t}{\Delta x} (\nabla \cdot F)_{\boldsymbol{i}}^{n+\frac{1}{2}} + \Delta t \, S_{\boldsymbol{i}}^{n+\frac{1}{2}}, \tag{69}$$

$$B_{d,\boldsymbol{i}+\frac{1}{2}\boldsymbol{e}^d}^{n+1} = \left(\frac{a^n}{a^{n+1}} \right)^{\frac{1}{2}} B_{d,\boldsymbol{i}+\frac{1}{2}\boldsymbol{e}^d}^n - \frac{1}{(a^{n+\frac{1}{2}} a^{n+1})^{\frac{1}{2}}} \frac{\Delta t}{\Delta x} (\boldsymbol{D} \times \boldsymbol{E})_{d,\boldsymbol{i}+\frac{1}{2}\boldsymbol{e}^d}^{n+\frac{1}{2}}, \tag{70}$$

where the time centered fluxes and electric fields, as well as the synchronization between face and cell centered magnetic field variables, are computed using the algorithm defined in Sec. 2. A second order estimate of the source term can be obtained by the simple time average $S^{n+\frac{1}{2}} \simeq \frac{1}{2}(S^n + S^{n+1})$. In reality, the source terms associated with gravity and expansion are implemented using a slightly more sophisticated method that estimates the change in kinetic energy due to the work by gravity, directly from the change in the momentum components. This is described in detail in Miniati & Colella (2007a). Similarly, after the face-centered magnetic field variables have been updated in time, the cell-centered values are synchronized, and the change in magnetic field energy due to cosmic expansion is computed from the corresponding change in the magnetic field components.

5.1.   MHD Santa Barbara Test

In this final test we present an MHD version of the 'Santa Barbara Cluster Comparison Project'. The tests consists of the formation of a massive cluster of galaxies in a 64 Mpc volume. The cosmological model is an Einstein-De Sitter universe (i.e. with critical total matter density) with 10% of the total matter density in baryons, and an expansion rate given by a Hubble parameter, $H_0 = 50$ km s^{-1} Mpc^{-1} (see additional details in Frenk et al. (1999)). The purpose of this calculation is to test our MHD solver in a realistic cosmological application. To compare with previously published results, the dynamic role of the magnetic field remains negligible throughout the calculation, which we ensure by adopting a sufficiently small initial magnetic seed. The geometry of such fields is immaterial, and is chosen to be uniform for convenience.

The calculation is performed basically as in Miniati & Colella (2007a), except for the initial redshift which is $z = 30$ (instead of 40). So, two initial grids are in place at simulation start: a base grid covering the entire 64 Mpc^3 domain with 64^3 cells and 64^3 particles; and a second grid, also with 64^3 cells and 64^3 particles, but only 32 Mpc on a side and placed in the central region of the base grid, thus yielding an initial cell size of 0.5 Mpc. Refinement is applied only within the latter higher resolution region to cells with a total mass larger than 6.4×10^{10} M$_\odot$. We allowed for 5 additional levels of refinement (for a total 6 level hierarchy), with a constant refinement ratio $n_{ref} = 2$. The size of the finest mesh is about 15 comoving kpc. The timestep is limited by the most stringent among the following three conditions: the Courant-Friedrichs-Lewy condition on the MHD waves, with coefficient $C_{\mathrm{CFL}} = 0.8$, an analogous CFL condition based on the speed of the collision-less particles, with coefficient $C_{\mathrm{part}} = 0.5$, and the requirement that the expansion of the universe during a time-step is less than 2%. The calculation was performed using the PPM reconstruction scheme and the

HLLD Riemann solver.

The results of the calculation are summarized by the radial plots in Fig. 16, where in analogy to Miniati & Colella (2007a) we show results from two other simulation codes. As expected, the MHD solver (in the limit of vanishing magnetic field) produces virtually the same results as the hydro solver in Miniati & Colella (2007a), attesting therefore to the same reliability for highly nonlinear calculations, involving high Mach number flows and large dynamic range in the fluid quantities. Finally, the left panel of Fig. 17 shows the magnetic field magnitude (in arbitrary units) distribution on a slice passing through the cluster center. The magnetic field is stronger in the core region where it also shows substantial spacial structure down to the smallest resolvable scales. On the left panel of the same Figure we present the distribution of the normalized magnetic field divergence, $|(\Delta x/B)\nabla B|$. The bulk of the distribution is at the level of 10^{-15} or so, and the max value is around 10^{-11}. Again, this value is completely negligible with respect to the solution value. While larger than the value obtained in the previous test example, this is expected given the much larger number of integration steps (about 10^4) in the current case.

6. Summary

We have presented the implementation of a three-dimensional scheme for MHD in the AMR code `CHARM`. The scheme uses a hybrid discretization, in the sense that fluid quantities are cell-centered, and magnetic field variables are face-centered. The algorithm is based on the full 12-solve spatially unsplit Corner-Transport-Upwind (CTU) scheme (Colella 1990). The fluid quantities are updated using the PPM method, while the magnetic field evolution is computed through a CT method. The edge-centered electric fields necessary for the CT step are computed as in Gardiner & Stone (2005). We employ a simplified version of the multidimensional MHD source terms required in the predictor step for high-order accuracy (Gardiner & Stone 2005, 2008), which is as in Crockett et al. (2005). This greatly simplifies the three-dimensional version of the algorithm with respect to the original form, without compromising the accuracy and robustness of the solutions.

The algorithm is implemented in an AMR framework. This requires synchronization operations across refinement levels, including face-centered restriction and prolongation operations and a reflux-curl operation, which is necessary to maintain a divergence-free magnetic field solution Balsara (2001). The code works with any even refinement ratio, although values above 4 are unusual. Our tests demonstrate that the code converges at the expected rate, is robust in problems involving strong shocks, maintains the magnetic field divergence at a negligible value and is suitable for astrophysical and cosmological applications.
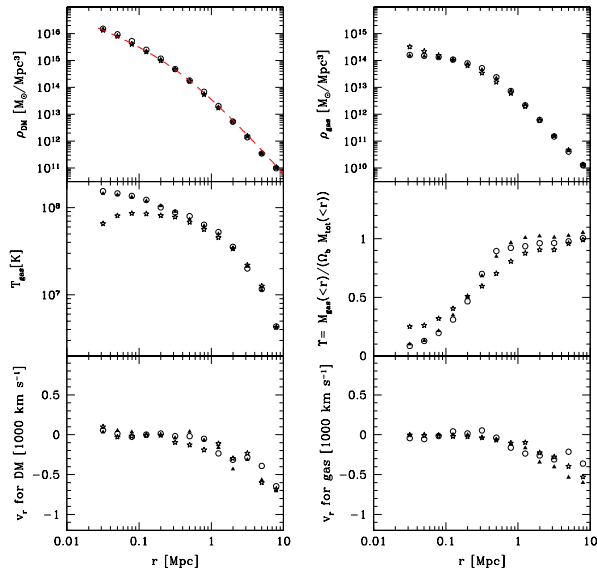
Fig. 16.— Radial profile of dark matter (top left), baryonic gas (top right) temperature (middle left), baryonic fraction (middle right), radial velocity for dark matter (bottom left) and gas (bottom right). In addition to the results from CHARM (open circles), for comparison we also show those from the ENZO AMR code (filled triangles) Bryan & Norman (1997) as well as those from the HYDRA SPH code (open stars) Couchman et al. (1995).

REFERENCES

Balsara, D. S. 2001, Journal of Computational Physics, 174, 614

Balsara, D. S., & Spicer, D. S. 1999, Journal of Computational Physics, 149, 270

Berger, M. J., & Colella, P. 1989, Journal of Computational Physics, 82, 64

Bernet, M. L., Miniati, F., Lilly, S. J., Kronberg, P. P., & Dessauges-Zavadsky, M. 2008, Nature, 454, 302

Brackbill, J. U., & Barnes, D. C. 1980, Journal of Computational Physics, 35, 426

Brio, M., & Wu, C. C. 1988, Journal of Computational Physics, 75, 400

Bryan, G. L., & Norman, M. L. 1997, in Computational Astrophysics, ed. D. A. Clarke & M. Fall, ASP Conference

Clarke, T. E., Kronberg, P. P., & Böhringer, H. 2001, ApJ, 547, L111

Colella, P. 1990, Journal of Computational Physics, 87, 171

Colella, P., & Woodward, P. R. 1984, Journal of Computational Physics, 54, 174

Couchman, H. M. P., Thomas, P. A., & Pearce, F. R. 1995, ApJ, 452, 797

Crockett, R. K., Colella, P., Fisher, R. T., Klein, R. I., & McKee, C. F. 2005, Journal of Computational Physics, 203, 422

Cunningham, A. J., Frank, A., Varnière, P., Mitran, S., & Jones, T. W. 2009, ApJS, 182, 519

Dai, W., & Woodward, P. R. 1998, ApJ, 494, 317

Dedner, A., Kemm, F., Kröner, D., Munz, C., Schnitzer, T., & Wesenberg, M. 2002, Journal of Computational Physics, 175, 645

Einfeldt, B., Roe, P. L., Munz, C. D., & Sjogreen, B. 1991, Journal of Computational Physics, 92, 273

Evans, C. R., & Hawley, J. F. 1988, ApJ, 332, 659

Frenk, C. S., White, S. D. M., Bode, P., Bond, J. R., Bryan, G. L., Cen, R., Couchman, H. M. P., Evrard, A. E., Gnedin, N., Jenkins, A., Khokhlov, A. M., Klypin, A., Navarro, J. F., Norman, M. L., Ostriker, J. P., Owen, J. M., Pearce, F. R., Pen, U. L., Steinmetz, M., Thomas, P. A., Villumsen, J. V., Wadsley, J. W., Warren, M. S., Xu, G., & Yepes, G. 1999, ApJ, 525, 554

Fromang, S., Hennebelle, P., & Teyssier, R. 2006, A&A, 457, 371

Gardiner, T. A., & Stone, J. M. 2005, Journal of Computational Physics, 205, 509

—. 2008, Journal of Computational Physics, 227, 4123

Ginzburg, V. L. 1979, Theoretical Physics and Astrophysics, International Series in Natural Philosophy (Oxford: Pergamon)

Gregori, G., Miniati, F., Ryu, D., & Jones, T. W. 1999, ApJ, 527, L113

—. 2000, ApJ, 543, 775

Jones, T. W., Ryu, D., & Tregillis, I. L. 1996, ApJ, 473, 365

Klein, R. I., McKee, C. F., & Colella, P. 1994, ApJ, 420, 213

Klein, R. I., McKee, C. F., & Woods, D. T. 1995, in Astronomical Society of the Pacific Conference Series, Vol. 80, The Physics of the Interstellar Medium and Intergalactic Medium, ed. A. Ferrara, C. F. McKee, C. Heiles, & P. R. Shapiro, 366–+

Landau, L. D., & Lifshitz, E. M. 1984, Course of Theoretical Physics, Vol. 8, Electrodynamics of Continuous Media, 2nd edn., ed. E. M. Lifshitz (Oxford: Pergamon Press)

Lattanzio, J. C., Monaghan, J. J., Pongracic, H., & Schwarz, M. P. 1985, MNRAS, 215, 125

Lee, D., & Deane, A. E. 2009, Journal of Computational Physics, 228, 952

Leveque, R. J. 1998, in Saas-Fee Advanced Course 27: Computational Methods for Astrophysical Fluid Flow., ed. O. Steiner & A. Gautschy, 1–+

Londrillo, P., & del Zanna, L. 2004, Journal of Computational Physics, 195, 17

Mac Low, M., McKee, C. F., Klein, R. I., Stone, J. M., & Norman, M. L. 1994, ApJ, 433, 757

Martin, D. F., & Colella, P. 2000, Journal of Computational Physics, 163, 271

Mignone, A., & Tzeferacos, P. 2010, Journal of Computational Physics, 229, 2117

Miniati, F. 2001, Computer Physics Communication, 141, 17

—. 2007, Journal of Computational Physics, 227, 776

—. 2010, Journal of Computational Physics, 229, 3916

Miniati, F., & Bell, A. R. 2011, ApJ, 729, 73

Miniati, F., & Colella, P. 2007a, Journal of Computational Physics, 227, 400

—. 2007b, Journal of Computational Physics, 224, 519

Miniati, F., Jones, T. W., Ferrara, A., & Ryu, D. 1997, ApJ, 491, 216

Miniati, F., Jones, T. W., & Ryu, D. 1999a, ApJ, 510, 726

Miniati, F., Ryu, D., Ferrara, A., & Jones, T. W. 1999b, ApJ, 517, 242

Miyoshi, T., & Kusano, K. 2005, Journal of Computational Physics, 208, 315

Neronov, A., & Vovk, I. 2010, Science, 328, 73

Orszag, S. A., & Tang, C. 1979, Journal of Fluid Mechanics, 90, 129

Powell, K. G., Roe, P. L., Linde, T. J., Gombosi, T. I., & de Zeeuw, D. L. 1999, Journal of Computational Physics, 154, 284

Roe, P. L., & Balsara, D. S. 1996, SIAM J. Appl. Math., 56, 57

Ryu, D., & Jones, T. W. 1995, ApJ, 442, 228

Ryu, D., Jones, T. W., & Frank, A. 1995, ApJ, 452, 785

Ryu, D., Miniati, F., Jones, T. W., & Frank, A. 1998, ApJ, 509, 244

Saltzman, J. 1994, Journal of Computational Physics, 115, 153

Samtaney, R., Colella, P., Ligocki, T. J., Martin, D. F., & Jardin, S. C. 2005, Journal of Physics Conference Series, 16, 40

Schiano, A. V. R., Christiansen, W. A., & Knerr, J. M. 1995, ApJ, 439, 237

Schlickeiser, R. 2002, Cosmic Ray Astrophysics

Spitzer, L. 1965, Physics of fully ionized gases, ed. Spitzer, L.

Stone, J. M., Gardiner, T. A., Teuben, P., Hawley, J. F., & Simon, J. B. 2008, ApJS, 178, 137

Teyssier, R., Fromang, S., & Dormy, E. 2006, Journal of Computational Physics, 218, 44

Tóth, G. 2000, Journal of Computational Physics, 161, 605

Vietri, M., Ferrara, A., & Miniati, F. 1997, ApJ, 483, 262

Yee, K. S. 1966, IEEE Transactions on Antennas and Propagation, 14, 302

Zachary, L. A., Malagoli, A., & Colella, P. 1994, SIAM J. Sci. Comput., 15, 263

Zel'dovich, Y. B., Ruzmaikin, A. A., & Sokoloff, D. D. 1983, The Fluid Mechanics of Astrophysics and Geophysics, Vol. 3, Magnetic Fields in Astrophysics, 2nd edn., ed. P. H. Roberts (New York: Gordon and Breach)
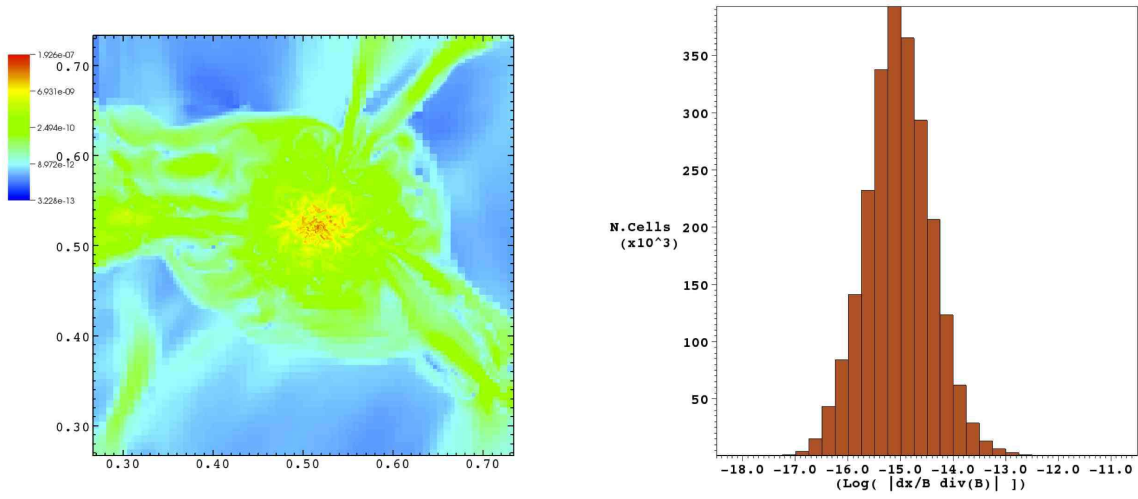
Fig. 17.— Left: Distribution of the magnetic field magnitude on a plane across the center of the simulated cluster. Right: Histogram of the absolute value of the normalized divergence of the magnetic field, $|(\Delta x/B)\nabla B|$.